

Serveur Académique Lausannois SERVAL serval.unil.ch

Author Manuscript

Faculty of Biology and Medicine Publication

This paper has been peer-reviewed but does not include the final publisher proof-corrections or journal pagination.

Published in final edited form as:

Title Local pheromone release from dynamic polarity sites underlies cell-cell pairing during yeast mating.

Authors:

Merlini L., Khalili B., Bendezú F.O., Hurwitz D., Vincenzetti V., Vavylonis D., Martin S.G.

Journal: Current Biology,

Year: 2016

Volume: 26(8)

Pages: 1117-1125

DOI: [10.1016/j.cub.2016.02.064](https://doi.org/10.1016/j.cub.2016.02.064)

In the absence of a copyright statement, users should assume that standard copyright protection applies, unless the article contains an explicit statement to the contrary. In case of doubt, contact the journal publisher to verify the copyright status of an article.

Local pheromone release from dynamic polarity sites underlies cell-cell pairing during yeast mating

Laura Merlini ¹&, Bitá Khalili ²&, Felipe O Bendezú ¹%, Daniel Hurwitz ^{2,3}% §,
Vincent Vincenzetti ¹, Dimitrios Vavylonis ²* and Sophie G Martin¹*

¹ University of Lausanne, Department of Fundamental Microbiology, Biophore Building, CH-1015 Lausanne, Switzerland

² Department of Physics, Lehigh University, Bethlehem, Pennsylvania 18015, USA

³ Department of Physics, University of Texas at Austin, Austin, Texas 78712, USA

§Current address: University of Texas Medical Branch in Galveston, Texas 77555, USA

& Co-first author

% Equal contribution

* Co-corresponding, Co-senior authors

Sophie G Martin: Sophie.Martin@unil.ch

Dimitrios Vavylonis: vavylonis@lehigh.edu

Summary

Cell pairing is central for many processes, including immune defense, neuronal connection, hyphal fusion or sexual reproduction. How does a cell orient towards a partner, especially when faced with multiple choices? Fission yeast *Schizosaccharomyces pombe* P- and M-cells, which respectively express P- and M-factor pheromones [1, 2], pair during the mating process induced by nitrogen starvation. Engagement of pheromone receptors Map3 and Mam2 [3, 4] with their cognate pheromone ligands leads to activation of the G α -protein Gpa1 to signal sexual differentiation [3, 5, 6]. Prior to cell pairing, the Cdc42 GTPase, a central regulator of cell polarization, forms dynamic zones of activity at the cell periphery at distinct locations over time [7]. Here, we show that Cdc42-GTP polarization sites contain the M-factor transporter Mam1, the general secretion machinery, which underlies P-factor secretion, and Gpa1, suggesting these are sub-cellular zones of pheromone secretion and signaling. Zone lifetimes scale with pheromone concentration. Computational simulations of pair formation through a fluctuating zone show that the combination of local pheromone release and sensing, short pheromone decay length, and pheromone-dependent zone stabilization leads to efficient pair formation. Consistently, pairing efficiency is reduced in absence of the P-factor protease. Similarly, zone stabilization at reduced pheromone levels, which occurs in absence of the predicted GTPase-activating protein for Ras, leads to reduction in pairing efficiency. We propose that efficient cell pairing relies on a fluctuating local signal emission and perception, which become locked into place through stimulation.

Results and Discussion

Local pheromone secretion and sensing in vivo

Previous modeling work of pheromone-dependent polarized growth in *S. cerevisiae* assumed that the cell serves as spherically uniform source of pheromone [8-12]. As the secretion machinery is normally polarized by Cdc42-GTP [13-16], an alternative likely scenario is that the pheromones are released locally at sites of polarization. We used live-cell imaging to probe the possible co-localization of components of the pheromone signaling machinery with dynamic Cdc42-GTP zones during ‘exploration’, i.e. after the last cell division upon nitrogen starvation but prior to polarized growth (also known as ‘shmoo’ formation; see [17] for review). To label Cdc42-GTP, we used tagged Scd2, a protein that links Cdc42 with its major guanine nucleotide exchange factor, and robustly co-localizes with Cdc42-GTP [7, 18, 19].

The M-factor pheromone is a lipid-modified peptide, exported outside the cell by a dedicated transporter, Mam1 (Figure 1A) [2, 20, 21]. Mam1-GFP signal was weak, but displayed local enrichment at cortical sites often coinciding with Scd2 zones (68 of 74 cells; Figure 1B, S1A-B), in addition to significant internal signal, likely due to endocytic recycling similar to its *S. cerevisiae* Ste6 homologue [22, 23]. This suggests M-factor is exported not around the entire cell cortex but locally, preferentially at sites of Cdc42 activity. As P-factor is a simple 23aa peptide, processed in the ER and Golgi, and likely secreted through the canonical secretory system (Figure 1A) [1], we monitored the localization of the secretion machinery by labeling the post-Golgi vesicle-associated Rab11-family GTPase Ypt3 [24, 25]. GFP-Ypt3 showed strong enrichment at Scd2 zones (67 of 75 cells; Figure 1C, S1C-D), similar to our previous description of both Myo52 myosin motor and exocyst complex at these zones [7]. These data indicate that both pheromones are preferentially released at Cdc42-GTP zones.

Engaged pheromone receptors signal through the associated G α -protein Gpa1 [5]. Because Gpa1 is predicted to be N-terminally myristoylated, we tagged it with mCherry at an internal poorly conserved site, generating Gpa1-mCherry^{SW}, integrated as sole copy at the endogenous *gpa1* genomic locus. These cells are fertile, although they exhibit reduced mating efficiencies (30% of cell pairing,

n=928 cells), indicating Gpa1-mCherry^{SW} is largely, but not completely functional. Gpa1-mCherry^{SW} fluorescence was weak, but could be detected at dynamic sites at the cell periphery, which often co-localized with Scd2 (45 of 63 cells; Figure 1D, S1E-F). By contrast, pheromone receptors were not exclusively associated with Scd2 zones, displaying instead a broad localization over the entire plasma membrane during exploration, as well as strong internal, likely endomembrane, localization (Figure 1E). This broad peripheral localization is consistent with the ability of cells to perceive a partner and extend a shmoo from any location [7]. During shmoo growth, receptors then became enriched at the shmoo site, as has been previously described in this and other species [26, 27] (Figure 1F). Because pheromone receptors are initially broadly distributed at the membrane, but their associated G α is enriched at specific sites, we interpret these sites of Gpa1 enrichment as sites of pheromone receptor engagement. The mechanisms of Gpa1 accumulation await future dissection. In summary, these results indicate that release and perception of pheromones occur at discrete cortical sites largely coincident with the dynamic zones of Cdc42 activity observed prior to cell pairing.

Simulation of cell pairing

To probe the logic behind the process of cell-cell pairing, we designed a simple numerical simulation mimicking an experimental two-dimensional field of cells of opposite mating types in a mating reaction. We implemented Cdc42-GTP zone (simply referred to as “zone” below) dynamics in each cell with a positional bias around cell poles, as measured experimentally [7]. The simulation is based on two simple assumptions. The first is that a zone lifetime scales with the local opposite-type pheromone concentration (Figure 2A). This assumption is validated by experimental observations: Heterothallic M-cells lacking the P-factor protease Sxa2 exposed to homogeneous low-level P-factor exhibit dynamic zones, with only high-level P-factor promoting polarized growth at a single site [7]. Furthermore, zone lifetimes increase with pheromone concentration ranging from 0.01 to 1 μ M (Figure 2B). We note that *S. cerevisiae* polarity site motility is also constrained by higher pheromone levels [28-30]. The

second assumption is that cells paired (i.e. with zones facing each other) for > 100 min have grown and fused together, and are thus taken out of the reaction (Figure 2C). Indeed, previous examination had shown that cells do not polarize towards fused pairs and readily re-orient if the target cell fuses with another partner [7]. The simulation relies on two parameters. The first, b , defines the linear response of the zone lifetime to the opposite type pheromone. For simplicity, we assume that this value is identical in the two distinct mating types. The second, λ , is the characteristic decay length of the pheromone signal [8, 9], which likely results from the action of secreted proteases that restrict it near the source [31-33].

Starting from a field of exploring cells (Figure 2D), the simulations lead to a pattern of cell pairing (Figure 2E) that varied in each realization due to the randomness of the exploration process (Movie S1). To monitor the success of the simulations, we quantified the fraction of paired cells over time and found the value of parameter b that gives the most efficient cell pairing for a given decay length λ (Figure 2F). The selected optimal value of b separates a high sensitivity regime where exploratory zones stabilize along unproductive orientations and a low sensitivity regime where cells spend most time exploring (Figure S2A-C; Movies S2 and S3).

In agreement with the local enrichment of pheromone secretion machineries at Cdc42-GTP zones, we found that local release of pheromones at the polarized patch (model 1) yielded more efficient pairing than global pheromone release (model 2) (Figure 2F). Consistently, low pheromone decay length allowed more efficient cell pairing (Figure 2F). Both models make the assumption that the pheromone signal is perceived at the site of the polarized patch, in agreement with local Gpa1 enrichment. As expected, decoupling pheromone perception from the polarized patch in the simulation (model 3) nearly blocked cell pairing (Figure 2F). Thus, the optimal conditions for efficient cell pairing in the simulation are local pheromone release and perception, as observed above, and pheromone decay length of order 1 μm or less. These results remained valid when considering configurations of cells that do not touch (Figure S2D-E), nonlinear response to pheromone concentration (Figure S2F-G) and cells

entering the exploratory phase over an extended time interval (Figure S2H-I). We also built a more detailed model accounting for the excluded cell volume in pheromone distributions. This detailed model recapitulated the more efficient cell pairing observed upon local pheromone release and pheromone decay length of order $1\mu\text{m}$ or less as in model 1 above (see supplementary text; Figure S2J-L). Because this model was very computationally expensive, we used the simple model below.

Simulation of cell pairing recapitulates experimental observations

To compare simulations to experiments, nitrogen-starved P and M cells were placed in a monolayer on a thin agarose pad at a density similar to that used in the simulations above (about $19'000$ cells per mm^2) and the fraction of paired cells was monitored over time. Up to 60% of cells became engaged in a pair and fused to form a zygote within 15h of starvation, with similar kinetics to that observed in the simulation with local pheromone release (Figure 2G-H).

To better define the efficiency of pairing, we focused on isolated small groups of cells, in which cells of distinct mating types were labeled with distinct fluorescence (Figure 3A). This small group analysis is interesting, because the low number of cells permits exact counting of all possible outcomes, including the optimal pairing configurations with the largest number of pairs. Remarkably, 77% of the cells mated, close to the maximum predictable efficiency of 83% that would have been obtained if the maximum number of pairs had been formed in each configuration (Figure 3A-B, where a different configuration could have yielded one more pair in each of experimental panels f and i). *In silico* arrangements of cells in small groups of identical distribution as those analyzed experimentally revealed comparable kinetics and pairing efficiency of $72 \pm 3\%$ (mean \pm stdev), with fluctuations due to the different partner choices occurring on each run of the simulation with local pheromone release (Figure 3A-B, where a different configuration could have yielded one more pair in each of simulation panels f and d; Movie S4). By contrast, we calculated that if each cell in the groups of Figure 2 made a single random choice among its possible partners, only $52 \pm 2\%$ of the cells would mate, with several cells making an

unreciprocated choice. If the cells with unreciprocated choices are allowed to make a second, third, or more choices, this increases the fraction of successful pairs to 74 ± 1.4 %, close to the realized value. Thus, the large fraction of pairs in simulations is realized through transient cell engagement followed by either simulated fusion or bond breakage. The same process can also be seen in time lapse images of *Scd2* zones of mating cells (Figure S3; [7]).

In conclusion, though we cannot exclude that pheromone concentration may also bias the site of zone assembly, our simulations suggest that efficient cell pairing is achieved through local pheromone release and sensing at dynamic zones that become stabilized by increased pheromone levels.

Deletion of P-factor protease reduces pairing efficiency

One prediction of the model is that optimal pairing occurs for pheromone decay lengths of order $1 \mu\text{m}$ or less. To test this prediction, we examined the ability of *sxa2Δ* M-cells to pair with wildtype P-cells. *Sxa2* is a secreted protease that cleaves P-factor, and thus likely contributes to shaping the pheromone landscape around cells [31-33], similar to the proposed role of *Bar1* protease in *S. cerevisiae* [8, 10]. In our 2D assay, the pairing efficiency of *h- sxa2Δ* x *h+ wt* crosses was reduced (Figure 4A, S4D), though interestingly not as dramatically as when assessed in 3D on agar plates ([31] and data not shown). Importantly, increasing the pheromone decay length of only a single partner, as in the *wt* x *sxa2Δ* crosses, also led to reduced pairing efficiency in simulations (Figure 4B).

The stronger phenotype of *sxa2Δ* mutants observed in 3D is in agreement with the idea that shaping of the pheromone gradients by the protease is particularly important when a large number of close partners each produce P-factor. To partly mimic this situation in 2D and further test the importance of pheromone concentration for cell-cell pairing, we added excess synthetic P-factor to fields of *wt* x *wt* or *sxa2Δ* x *wt* crosses, with the aim to further “confuse” the cell as to the origin of the pheromone gradient [34, 35]. Addition of $10\mu\text{g/ml}$ synthetic P-factor led to a partial decrease in pairing efficiency in *wt* crosses, but to a strong impairment in *sxa2Δ* x *wt* crosses, in which the excess P-factor cannot be

degraded, and resulted in the majority of cells growing unproductive, unpaired projections (Figure 4A, S4D). In simulations, we mimicked the predicted increased zone lifetime due to the homogeneous higher P-factor concentration by increasing the overall patch lifetime, τ_0 , in M cells (while keeping $b\tau_0$ constant to maintain the same level of sensitivity; see supplemental text). This led to a decrease in pairing efficiency, which appeared additive rather than synergistic with the effect of increased P-factor decay length (Figure 4B). This is likely because the fate of the added synthetic pheromone is different in wildtype, where it is progressively degraded, than in *sxa2Δ* mutants, where its concentration remains high throughout the experiment. Additional increase of τ_0 in the simulation indeed further lowered pairing efficiency, better mimicking the *wt x sxa2Δ* experimental situation (Figure 4B). We conclude that experiments and simulations are in agreement that short pheromone decay lengths are critical for efficient cell pairing.

Increasing zone lifetime reduces mating efficiency

We then sought to experimentally modify the internal cell mechanisms determining zone lifetime and its dependence to pheromone concentration, thus varying the equivalent of parameters τ_0 and b in the model. The molecular mechanisms underlying oscillations of Cdc42-GTP zones in response to pheromone are not well defined, but the small GTPase Ras1 is a likely important factor [17]. Indeed, Ras activity requires and in turn promotes pheromone signaling [36-38]. Ras was also proposed to be a positive regulator of Scd1, the major guanine nucleotide exchange factor activating Cdc42 [19]. Consistent with this idea, we found that *ras1Δ* cells failed to recruit Scd1 to the cell cortex during mating and formed broad zones of Scd2 polarization that did not dynamically explore the cell cortex (Figure S4A-B). N-terminally tagged GFP-Ras1 also accumulated at sites of Scd2 dynamic exploration, though it was also present at other cortical regions (Figure S4C). Thus, Ras1 is a likely positive regulator of local Cdc42 activation during exploratory polarization.

A zone lifetime is likely modulated by negative signals promoting zone disassembly. Indeed, deletion of Gap1, the predicted GTPase activating protein

(GAP) for Ras1 [39, 40], caused an important increase in zone lifetime: heterothallic *gap1Δ* M-cells lacking the P-factor protease Sxa2 exposed to homogeneous P-factor (0.01 to 1μM) displayed dynamic Scd2 zones, but these exhibited significantly longer lifetimes than *gap1+* controls exposed to the same pheromone concentrations (Figure 4C). Some of these cells also lysed, as previously reported [40]. Thus, Ras inactivation promotes polarity zone disassembly.

The *gap1Δ* mutant represents a condition in which cells exhibit an apparent increase in the parameters τ_0 and b . As predicted in simulations with increased τ_0 and b for one cell type, *wt x gap1Δ* formed pairs with significantly reduced efficiency, with *gap1Δ* cells stabilizing a growth axis at unreciprocated locations (Figure 4D-E, S4D). The stronger phenotype observed experimentally may stem from the formation of these unpaired projections, as well as from the lysis of some *gap1Δ* cells. Indeed, modification of the simulation to remove cells with zones stable for >200min better mimicked the experimental situation (Figure 4E). Thus, reducing the pheromone concentration-dependency for zone stabilization prevents transient engagements and locks polarity zones in inappropriate locations. We conclude that an optimal zone lifetime, stabilized only by high concentrations of pheromone, is required for efficient cell-cell pairing.

Conclusion

We propose that local pheromone signal release and perception underlies flexible cell-cell communication for efficient pair formation. Our experimental data indicate that exploratory polarity sites represent discrete zones of localized pheromone signal release and sensing, and our computational approach demonstrates that fluctuating local signal emission and perception, which becomes locked into place through stimulation, serves for optimal pairing of cells during yeast mating. The fluctuating nature of the zones of signal release and perception is critical to this process, as demonstrated by the inefficient pairing of *gap1Δ* cells, in which polarity zones are stabilized at significantly lower pheromone concentrations. The short decay length of the pheromone gradient

highlighted in the simulations is consistent with the short range of fission yeast cell mating and validated by the lower pairing efficiency of *sxa2Δ* cells. We note that we observed similar reduction in pair formation with P-cells lacking Sxa1, a predicted M-factor protease [31]. A prior calculation suggested that a very high concentration of diffuse proteases would be needed to restrict the pheromone concentration profile to scales of order one cell diameter [9]. While some proteases may not be freely diffusing, we note that an increase in nonlinear sensitivity to pheromone concentration (parameter n) gives a similar trend to that of decreasing pheromone decay length (compare Figure 3B to Figure S2F, G). Thus nonlinear sensitivity to pheromone concentration could be an additional mechanism that cells use to effectively achieve local sensing. We also note that we assumed spatially uniform protease activity to highlight the effects of local pheromone secretion and decay length, however non-uniform protease activity over scales comparable to the cell size may also contribute to the mating kinetics [9].

The pheromone gradient sensing mechanism proposed here has features of sensing by temporal averaging [41], since exploratory zones localize in regions of higher pheromone concentration on average. More than just contributing to gradient sensing, fluctuations in the position of the zone also lead to different transient cell engagements. This mechanism of partner switching that would not be possible through local zone wandering [28-30] allows the cell population to test different conflicting mating configurations (reminiscent of the configurations of frustrated physical systems with quenched disorder [42]). This non-deterministic conceptual pairing framework may be valid beyond yeast sex, for instance for the formation of connections in filamentous fungal mycelia [43] or for activity-dependent stabilization of neuronal connections [44].

Experimental procedures

Strains, Media, and Growth Conditions

S. pombe strains used are listed in Table S1. Standard *S. pombe* media and genetic manipulations were used [45]. For all mating experiment cells were grown in MSL ± N (minimal sporulation medium with or without nitrogen), as described [7, 46]. For construction of *gpa1-mCherry^{sw}-kanMX4* a mCherry fusion was inserted after amino acid S132 at endogenous genomic locus. GFP-Ypt3 was expressed from plasmid (pREP41-GFP-Ypt3) under the control of *nmt41* promoter, as described [24]. Further details are provided in the supplementary file.

Microscopy and Image Analysis

Images in Figures 2, 3, 4, S3 and S4A, B, D were acquired on a DeltaVision epifluorescence system. The DeltaVision platform (Applied Precision) was composed of a customized Olympus IX-71 inverted microscope and a Plan Apo 60×/1.42 NA (for DIC) or a U-Plan Apo 100×/1.4 NA oil objective (for fluorescence), a CoolSNAP HQ2 camera (Photometrics), and an Insight SSI 7 color combined unit illuminator. To limit photobleaching, images were captured by OAI (optical axis integration).

High-resolution imaging in Figures 1, S1 and S4C was performed on a spinning disk confocal microscope. Optical slices were acquired every 0.6 μm and maximum projections are shown.

Peripheral kymographs were constructed in ImageJ v1.46 by drawing a 3 pixel-wide line around the cell cortex.

All imaging was performed at room temperature (20-22°C). Figures were assembled with Adobe Photoshop CS5 and Adobe Illustrator CS5.

Author Contributions

LM, FOB, VV and SGM performed experiments and analyzed data. BK, DH and DV developed and performed numerical simulations. LM and BK, and FOB and DH contributed equally to the work, respectively. SGM and DV wrote the manuscript.

Acknowledgements

This work was supported by a Swiss National Science Foundation (SNF) research grant (31003A_138177) and a Marie Curie Initial Training Network (FUNGIBRAIN) to SGM, NIH grant R01GM098430 to DV, and an SNF International Short Visit grant to SGM and DV. DH was supported by the National Science Foundation Research Experience for Undergraduates site grant PHY-1359195 at Lehigh University.

References

1. Imai, Y., and Yamamoto, M. (1994). The fission yeast mating pheromone P-factor: its molecular structure, gene structure, and ability to induce gene expression and G1 arrest in the mating partner. *Genes Dev* 8, 328-338.
2. Davey, J. (1992). Mating pheromones of the fission yeast *Schizosaccharomyces pombe*: purification and structural characterization of M-factor and isolation and analysis of two genes encoding the pheromone. *EMBO J* 11, 951-960.
3. Tanaka, K., Davey, J., Imai, Y., and Yamamoto, M. (1993). *Schizosaccharomyces pombe* map3+ encodes the putative M-factor receptor. *Mol Cell Biol* 13, 80-88.
4. Kitamura, K., and Shimoda, C. (1991). The *Schizosaccharomyces pombe* mam2 gene encodes a putative pheromone receptor which has a significant homology with the *Saccharomyces cerevisiae* Ste2 protein. *Embo J* 10, 3743-3751.
5. Obara, T., Nakafuku, M., Yamamoto, M., and Kaziro, Y. (1991). Isolation and characterization of a gene encoding a G-protein alpha subunit from *Schizosaccharomyces pombe*: involvement in mating and sporulation pathways. *Proc Natl Acad Sci U S A* 88, 5877-5881.
6. Xu, H.P., White, M., Marcus, S., and Wigler, M. (1994). Concerted action of RAS and G proteins in the sexual response pathways of *Schizosaccharomyces pombe*. *Mol Cell Biol* 14, 50-58.
7. Bendezu, F.O., and Martin, S.G. (2013). Cdc42 Explores the Cell Periphery for Mate Selection in Fission Yeast. *Curr Biol* 23, 42-47.

8. Barkai, N., Rose, M.D., and Wingreen, N.S. (1998). Protease helps yeast find mating partners. *Nature* 396, 422-423.
9. Rappaport, N., and Barkai, N. (2012). Disentangling signaling gradients generated by equivalent sources. *Journal of biological physics* 38, 267-278.
10. Jin, M., Errede, B., Behar, M., Mather, W., Nayak, S., Hasty, J., Dohlman, H.G., and Elston, T.C. (2011). Yeast dynamically modify their environment to achieve better mating efficiency. *Science signaling* 4, ra54.
11. Diener, C., Schreiber, G., Giese, W., del Rio, G., Schroder, A., and Klipp, E. (2014). Yeast mating and image-based quantification of spatial pattern formation. *PLoS Comput Biol* 10, e1003690.
12. Andrews, S.S., Addy, N.J., Brent, R., and Arkin, A.P. (2010). Detailed simulations of cell biology with Smoldyn 2.1. *PLoS Comput Biol* 6, e1000705.
13. Estravis, M., Rincon, S.A., Santos, B., and Perez, P. (2011). Cdc42 regulates multiple membrane traffic events in fission yeast. *Traffic* 12, 1744-1758.
14. Bendezu, F.O., and Martin, S.G. (2011). Actin cables and the exocyst form two independent morphogenesis pathways in the fission yeast. *Mol Biol Cell* 22, 44-53.
15. Martin, S.G., and Arkowitz, R.A. (2014). Cell polarization in budding and fission yeasts. *FEMS microbiology reviews* 38, 228-253.
16. Martin, S.G., Rincon, S.A., Basu, R., Perez, P., and Chang, F. (2007). Regulation of the formin for3p by cdc42p and bud6p. *Mol Biol Cell* 18, 4155-4167.
17. Merlini, L., Dudin, O., and Martin, S.G. (2013). Mate and fuse: how yeast cells do it. *Open biology* 3, 130008.
18. Bendezu, F.O., Vincenzetti, V., Vavylonis, D., Wyss, R., Vogel, H., and Martin, S.G. (2015). Spontaneous Cdc42 polarization independent of GDI-mediated extraction and actin-based trafficking. *PLoS Biol* 13, e1002097.
19. Chang, E.C., Barr, M., Wang, Y., Jung, V., Xu, H.P., and Wigler, M.H. (1994). Cooperative interaction of *S. pombe* proteins required for mating and morphogenesis. *Cell* 79, 131-141.
20. Kjaerulff, S., Davey, J., and Nielsen, O. (1994). Analysis of the structural genes encoding M-factor in the fission yeast *Schizosaccharomyces pombe*: identification of a third gene, *mfm3*. *Mol Cell Biol* 14, 3895-3905.
21. Christensen, P.U., Davey, J., and Nielsen, O. (1997). The *Schizosaccharomyces pombe* *mam1* gene encodes an ABC transporter mediating secretion of M-factor. *Mol Gen Genet* 255, 226-236.
22. Kolling, R., and Hollenberg, C.P. (1994). The ABC-transporter Ste6 accumulates in the plasma membrane in a ubiquitinated form in endocytosis mutants. *EMBO J* 13, 3261-3271.
23. Kelm, K.B., Huyer, G., Huang, J.C., and Michaelis, S. (2004). The internalization of yeast Ste6p follows an ordered series of events involving phosphorylation, ubiquitination, recognition and endocytosis. *Traffic* 5, 165-180.
24. Lo Presti, L., and Martin, S.G. (2011). Shaping fission yeast cells by rerouting actin-based transport on microtubules. *Curr Biol* 21, 2064-2069.

25. Cheng, H., Sugiura, R., Wu, W., Fujita, M., Lu, Y., Sio, S.O., Kawai, R., Takegawa, K., Shuntoh, H., and Kuno, T. (2002). Role of the Rab GTP-binding protein Ypt3 in the fission yeast exocytic pathway and its connection to calcineurin function. *Mol Biol Cell* *13*, 2963-2976.
26. Hirota, K., Tanaka, K., Watanabe, Y., and Yamamoto, M. (2001). Functional analysis of the C-terminal cytoplasmic region of the M-factor receptor in fission yeast. *Genes Cells* *6*, 201-214.
27. Jackson, C.L., Konopka, J.B., and Hartwell, L.H. (1991). *S. cerevisiae* alpha pheromone receptors activate a novel signal transduction pathway for mating partner discrimination. *Cell* *67*, 389-402.
28. Hegemann, B., Unger, M., Lee, S.S., Stoffel-Studer, I., van den Heuvel, J., Pelet, S., Koepl, H., and Peter, M. (2015). A Cellular System for Spatial Signal Decoding in Chemical Gradients. *Dev Cell* *35*, 458-470.
29. McClure, A.W., Minakova, M., Dyer, J.M., Zyla, T.R., Elston, T.C., and Lew, D.J. (2015). Role of Polarized G Protein Signaling in Tracking Pheromone Gradients. *Dev Cell* *35*, 471-482.
30. Dyer, J.M., Savage, N.S., Jin, M., Zyla, T.R., Elston, T.C., and Lew, D.J. (2012). Tracking Shallow Chemical Gradients by Actin-Driven Wandering of the Polarization Site. *Curr Biol*.
31. Imai, Y., and Yamamoto, M. (1992). *Schizosaccharomyces pombe* *sxa1+* and *sxa2+* encode putative proteases involved in the mating response. *Mol Cell Biol* *12*, 1827-1834.
32. Ladds, G., and Davey, J. (2000). *Sxa2* is a serine carboxypeptidase that degrades extracellular P-factor in the fission yeast *Schizosaccharomyces pombe*. *Mol Microbiol* *36*, 377-390.
33. Ladds, G., Rasmussen, E.M., Young, T., Nielsen, O., and Davey, J. (1996). The *sxa2*-dependent inactivation of the P-factor mating pheromone in the fission yeast *Schizosaccharomyces pombe*. *Mol Microbiol* *20*, 35-42.
34. Jackson, C.L., and Hartwell, L.H. (1990). Courtship in *S. cerevisiae*: both cell types choose mating partners by responding to the strongest pheromone signal. *Cell* *63*, 1039-1051.
35. Dorer, R., Pryciak, P.M., and Hartwell, L.H. (1995). *Saccharomyces cerevisiae* cells execute a default pathway to select a mate in the absence of pheromone gradients. *J Cell Biol* *131*, 845-861.
36. Hughes, D.A., Yabana, N., and Yamamoto, M. (1994). Transcriptional regulation of a Ras nucleotide-exchange factor gene by extracellular signals in fission yeast. *J Cell Sci* *107 (Pt 12)*, 3635-3642.
37. Nadin-Davis, S.A., Nasim, A., and Beach, D. (1986). Involvement of ras in sexual differentiation but not in growth control in fission yeast. *Embo J* *5*, 2963-2971.
38. Hughes, D.A., Fukui, Y., and Yamamoto, M. (1990). Homologous activators of ras in fission and budding yeast. *Nature* *344*, 355-357.
39. Imai, Y., Miyake, S., Hughes, D.A., and Yamamoto, M. (1991). Identification of a GTPase-activating protein homolog in *Schizosaccharomyces pombe*. *Mol Cell Biol* *11*, 3088-3094.
40. Weston, C., Bond, M., Croft, W., and Ladds, G. (2013). The coordination of cell growth during fission yeast mating requires Ras1-GTP hydrolysis. *PLoS One* *8*, e77487.

41. Endres, R.G. (2013). *Physical principles in sensing and signaling: with an introduction to modeling in biology* (Oxford University Press).
42. Binder, K., and Young, A.P. (1986). Spin-Glasses - Experimental Facts, Theoretical Concepts, and Open Questions. *Rev Mod Phys* *58*, 801-976.
43. Read, N.D., Lichius, A., Shoji, J.Y., and Goryachev, A.B. (2009). Self-signalling and self-fusion in filamentous fungi. *Curr Opin Microbiol* *12*, 608-615.
44. Okawa, H., Hoon, M., Yoshimatsu, T., Della Santina, L., and Wong, R.O. (2014). Illuminating the multifaceted roles of neurotransmission in shaping neuronal circuitry. *Neuron* *83*, 1303-1318.
45. Moreno, S., Klar, A., and Nurse, P. (1991). Molecular genetic analysis of fission yeast *Schizosaccharomyces pombe*. *Methods in enzymology* *194*, 795-823.
46. Vjestica, A., Merlini, L., Dudin, O., Bendezu, F.O., and Martin, S.G. (in press). Microscopy of Fission Yeast Sexual Lifecycle. *Journal of Vizualized Experiments*.

Figure legends

Figure 1. Localization of the pheromone release and sensing machineries at polarized zones.

(A) Schematic of the main pheromone secretion and sensing components in the two fission yeast mating types. (B-F) Transmitted light images and spinning disk confocal projections of *h90* wild-type strains showing co-localization of Scd2-mCherry and Mam1-GFP (B), Scd2-mCherry and GFP-Ypt3 (C), Scd2-GFP and Gpa1-mCherry^{sw} (D), Scd2-mCherry and Mam2-sfGFP (E, F). Kymographs of the cell periphery are shown on the right (B-D). Arrowheads highlight dynamic zones of co-localization. See Figure S1 for additional co-localization images and kymographs. Scale bars are 5 μm .

Figure 2. Model and experiment of fission yeast mating kinetics.

(A) Schematic of three mechanisms for pheromone secretion and sensing. A P (*h+*) cell is shown in blue, secreted pheromone (P-factor) in light blue, Cdc42-GTP patch in red, and region of sensing indicated by black receptors. Model 1: Local pheromone secretion and local sensing of opposite pheromone; Model 2: Uniform pheromone secretion and local sensing of opposite pheromone; Model 3: Local pheromone secretion and uniform sensing of opposite pheromone. For each model the corresponding equation of Cdc42 patch lifetime τ is shown. For Models 1 and 2, τ depends on the concentration of M-factor at the patch position r_{patch} , while in model 3 τ depends on the average concentration of M-factor around the cell perimeter. (B) Dependency of patch lifetime on pheromone concentration. *h- sxa2Δ scd2-GFP* cells were exposed to indicated amounts of P-factor and the lifetime of Scd2 cortical zones was measured in 25 cells for each condition (n = 135; 112; 87; 37 zones for 0.001; 0.01; 0.1 and 1 $\mu\text{g}/\text{ml}$ P-factor, respectively). (C) Cells in the simulation mate if they become mutually engaged for a time longer than $\tau_{\text{pairing}} = 100$ min. Cells are considered engaged if an opposite mating type patch is within a selection zone, representing the region over which a shmoo would be able to grow. Blue and pink cells represent P and

M cells, respectively. (D) Example of snapshot of simulations at $t = 0$ and the corresponding pheromone concentration field for $\lambda = 3 \mu\text{m}$. (E) Snapshot of the same simulation as panel D after 2000 min. Arrows show final pairing results. See movie S1. (F) Fraction of paired cells vs. time for the three models, for different decay lengths λ . Each line shows the average of 100 runs of 36 cells of random mating type, placed at random locations (for each run). Each curve shows the results obtained with a value b to within 10% of the optimal value that gives the most efficient pairing. (Model 1: $\lambda = 0.3 \mu\text{m}$: $b\phi_0 = 55000$; $\lambda = 1 \mu\text{m}$: $b\phi_0 = 2000$; $\lambda = 3 \mu\text{m}$: $b\phi_0 = 1500$. Model 2: $\lambda = 0.3 \mu\text{m}$: $b\phi_0 = 1050$; $\lambda = 1 \mu\text{m}$: $b\phi_0 = 100$; $\lambda = 3 \mu\text{m}$: $b\phi_0 = 40$. Model 3: $\lambda = 1 \mu\text{m}$: $b\phi_0 = 7000$.) See Figure S2 and movies S2 and S3 for further analysis of model parameters. (G) DIC images of representative fields of cells at the beginning and end of a two-dimensional mating experiment on agarose pad as in (H). Scale bar is $5\mu\text{m}$. (H) Cell-cell pairing kinetics of a population of mating cells ($n=3$ experiments, >800 cells each). P and M cells were mixed 1:1, shifted to MSL-N for 4h, spotted on MSL-N agarose pad for 1h and imaged for 12h. Time 0 indicates the start of imaging, 5h after starvation.

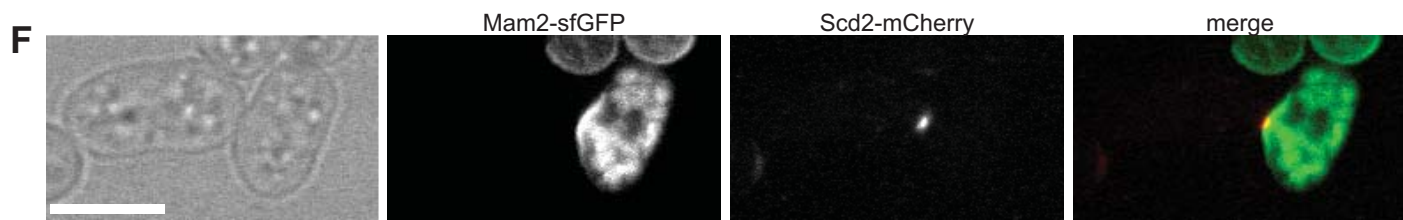
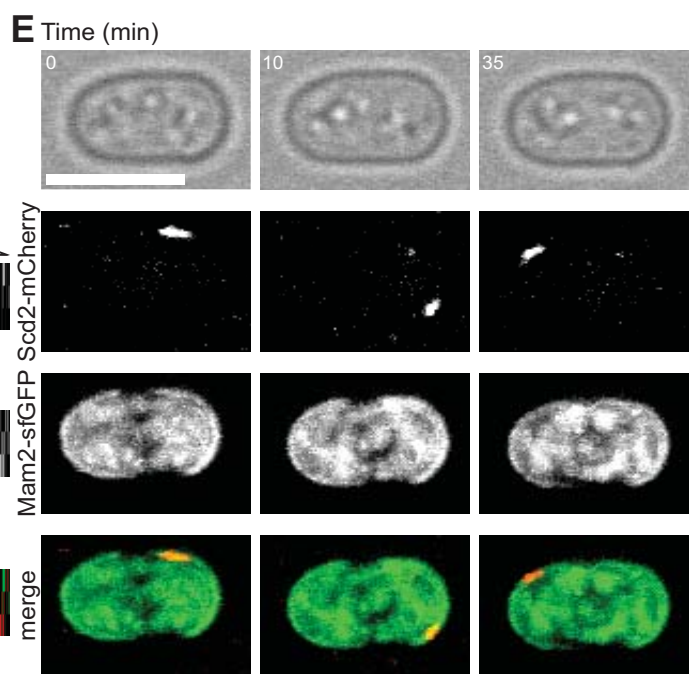
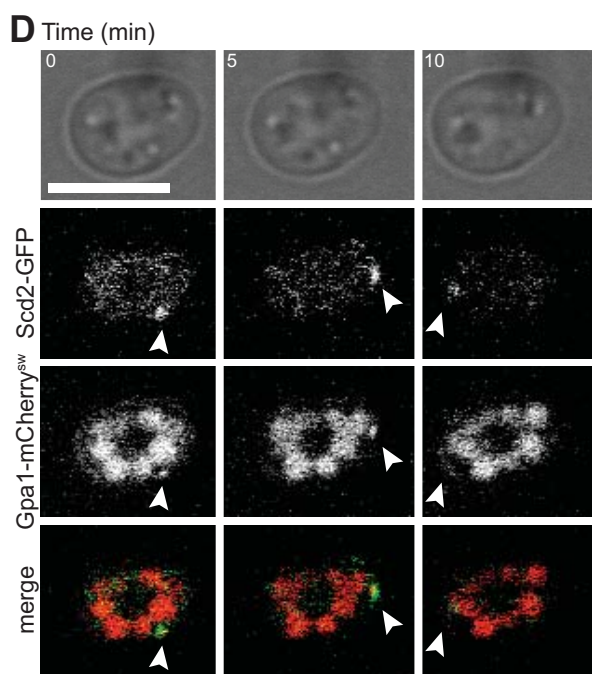
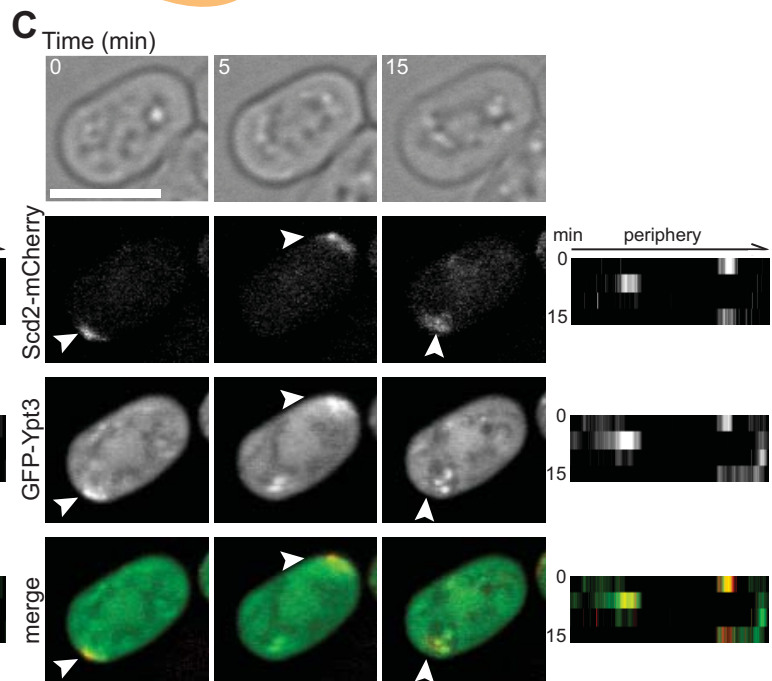
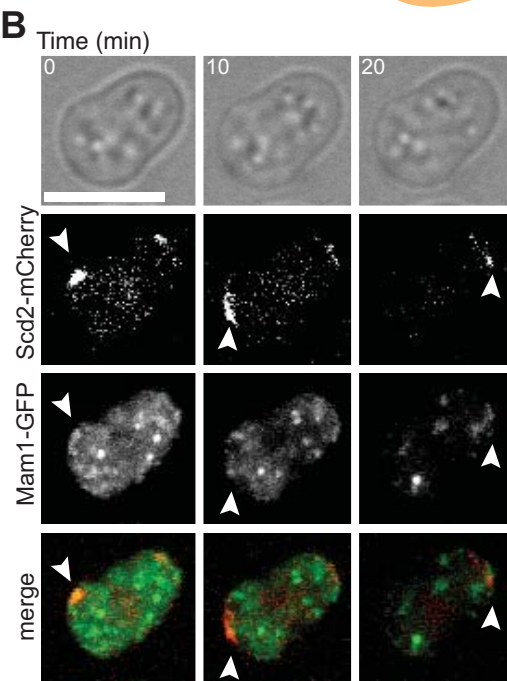
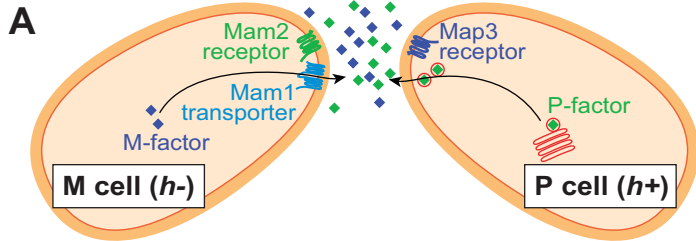
Figure 3. Cell-cell pairing occurs efficiently in fission yeast.

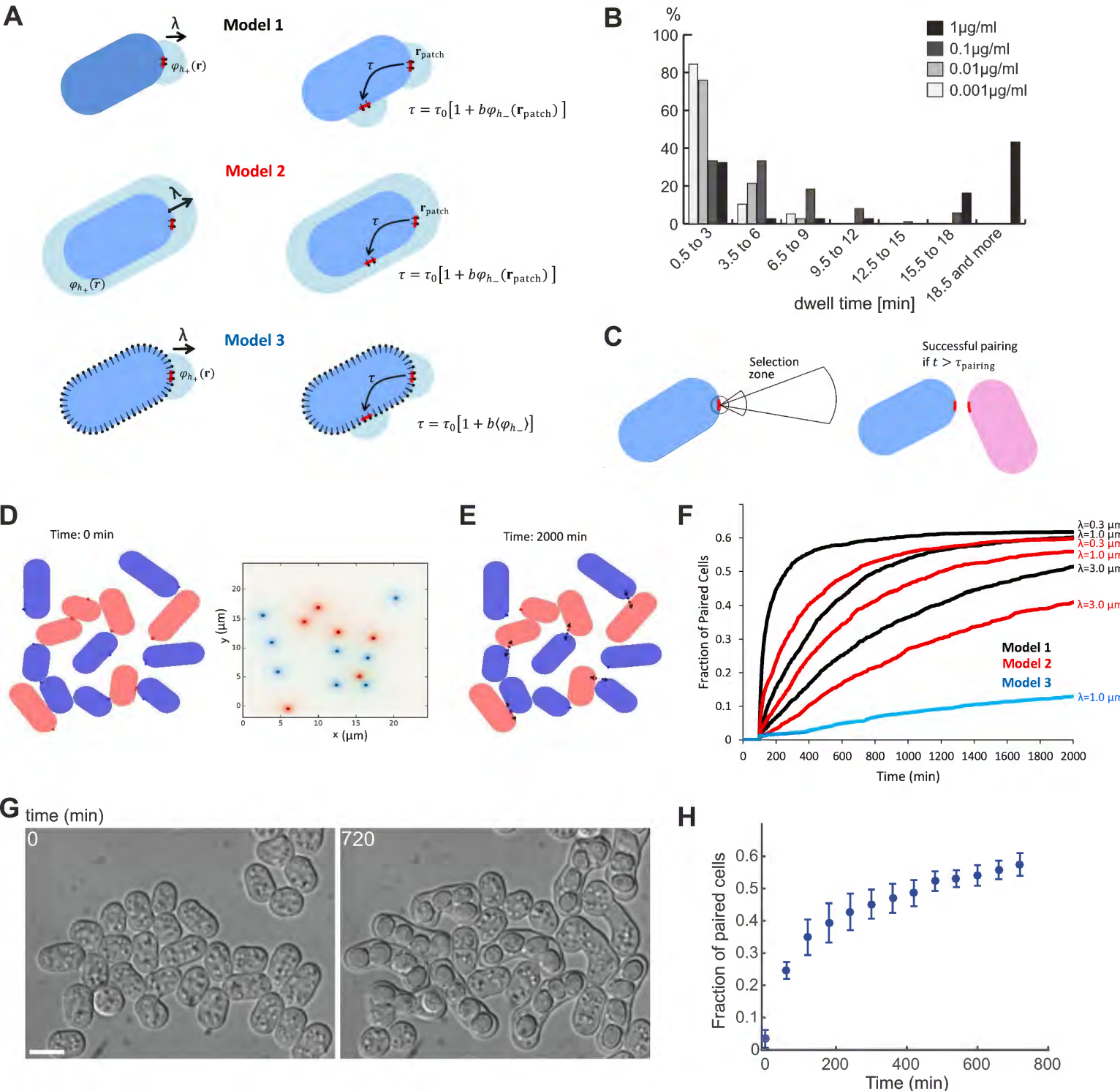
(A) DIC images showing examples of small groups of cells pairing (+ = P-cells, - = M-cells) at the beginning and the end of the experiment. P and M cells were mixed 1:1, shifted to MSL-N for 4h, spotted on MSL-N agarose pad for 1h and imaged for 12h. P cells express Scd1-3GFP and M cells express Scd2-mCherry to distinguish the mating type (not shown). Scale bars are $5 \mu\text{m}$. The images on the right are examples of simulation results of similar groups of cells. P cells are shown in blue, M cells are shown in pink, arrows indicate the final pairing configuration. The percentages show the probability of observing the displayed mating pattern in 25 runs. The percentages in brackets show the probability of finding the experimental mating pattern in simulations, for those cases where the shown simulation outcome differs from experiment. See Movie S4 for the animation as in panel d, and Figure S3 for experimental timelapse imaging of polarity zones. (B) Cell-cell pairing kinetics of the small groups of cells as in (A)

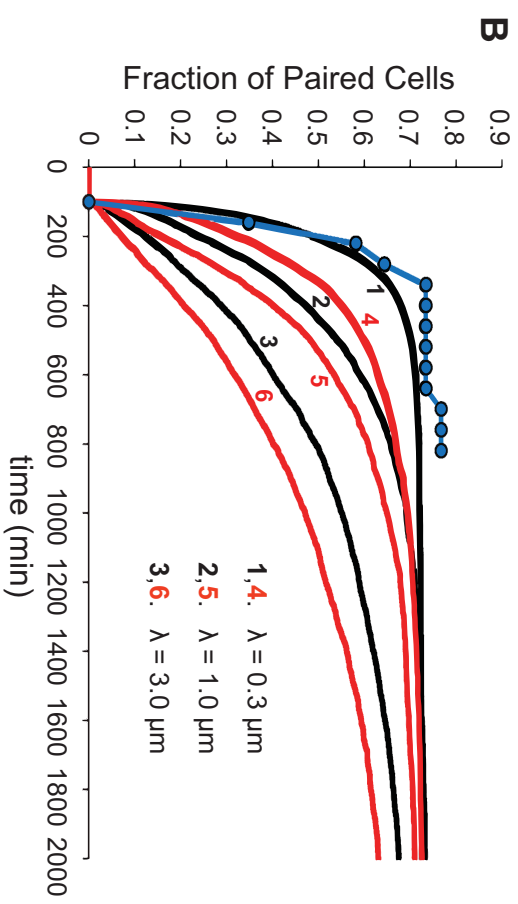
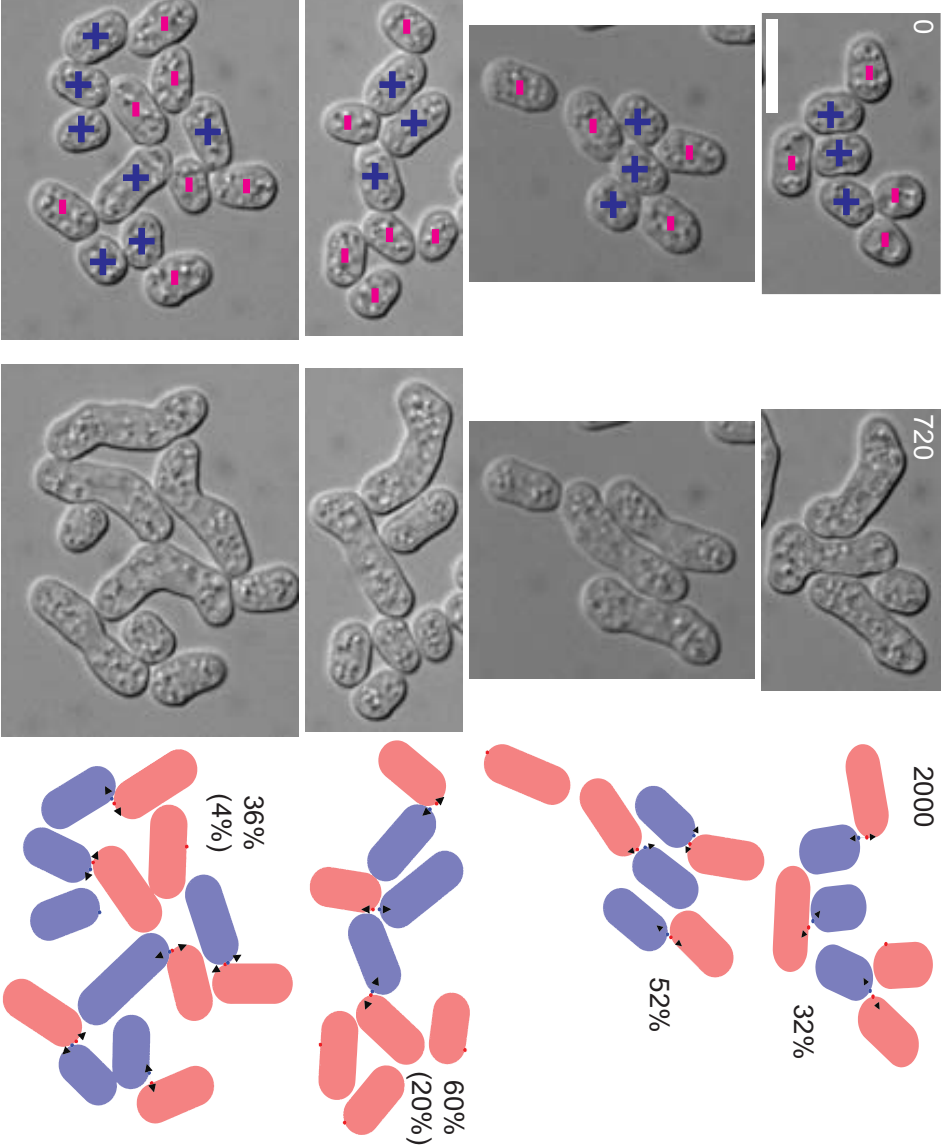
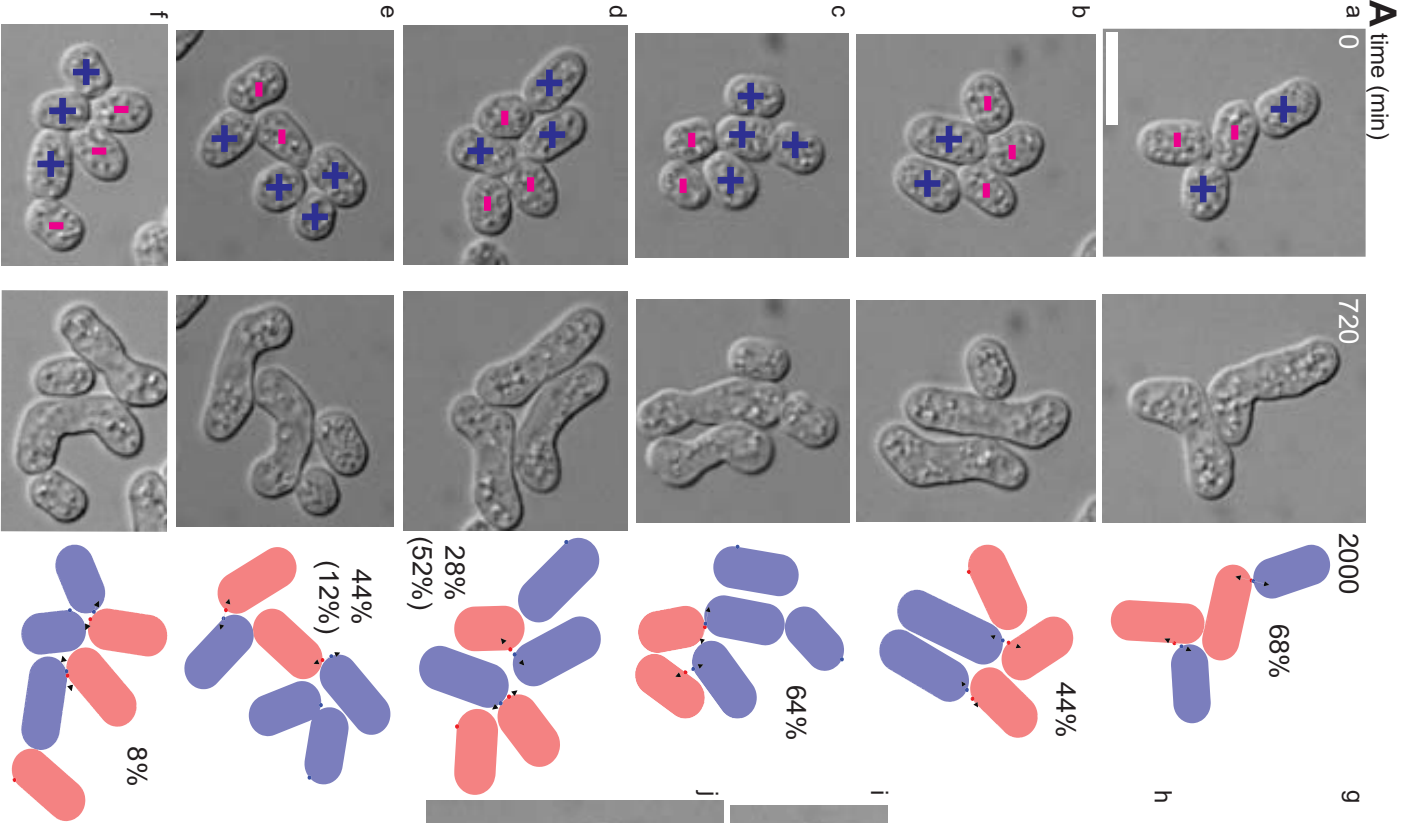
(blue curve) or resulting from *in silico* simulations (black and red curves, corresponding to Model 1 and 2 of Figure 1, respectively). Note that the time 0 of the experimental curve (i.e. start of imaging) was aligned to the 100min time of the simulation curves. Curves show the average of 100 simulations, each with all the shown small cell groups. Results use the optimal sensitivity parameter for this configuration, calculated as in Figure 1F (Model 1: $\lambda = 0.3 \mu\text{m}$: $b\varphi_0 = 15000$; $\lambda = 1 \mu\text{m}$: $b\varphi_0 = 3000$; $\lambda = 3 \mu\text{m}$: $b\varphi_0 = 1000$. Model 2: $\lambda = 0.3 \mu\text{m}$: $b\varphi_0 = 1050$; $\lambda = 1 \mu\text{m}$: $b\varphi_0 = 100$; $\lambda = 3 \mu\text{m}$: $b\varphi_0 = 40$).

Figure 4: Increased pheromone decay length and sensitivity impair cell-cell pairing

(A) Cell-cell pairing kinetics of *wt* mated with *wt* or *sxa2Δ* mutant cells (n=3 experiments, >800 cells each), treated as in Figure 2H. (B) Fraction of paired cells vs. time in simulations using Model 1, calculated as in Figure 2F. The wild type reference values are $\lambda = 1 \mu\text{m}$, $\tau_0 = 1.5$ and optimal b for *wt* x *wt* simulation. The values of λ corresponding to P-factor and τ_0 of *h-* cells were varied as indicated, adjusting b each time such that $b\tau_0$ is unchanged (see Equation (2) of supplemental text). (C) *gap1Δ* cells exhibit longer zone lifetimes than *gap1+* cells. Experiment and data as in Figure 2B, comparing *h- sxa2Δ scd2-GFP* with *h- sxa2Δ gap1Δ scd2-GFP* cells (n = 77; 56; 28; 29 zones in *gap1Δ* cells for 0.001; 0.01; 0.1 and 1 $\mu\text{g/ml}$ P-factor, respectively). Data in Figure S4A-C shows the role of Ras1 in zone exploration. (D) Cell-cell pairing kinetics of *wt* x *gap1Δ* mutant cells (n=3 experiments, >800 cells each), treated as in Figure 2H. (E) Fraction of simulated paired cells vs. time, with values of τ_0 and b for M-cells estimated from the zone residence times and response to pheromone of *gap1Δ* cells in panel C. Cells with zones stable for more than 200 min were taken out of the simulation for the results of the indicated curves, to account for lysis and unreciprocated shmoos. See Figure S4D for representative images of mating cell fields.







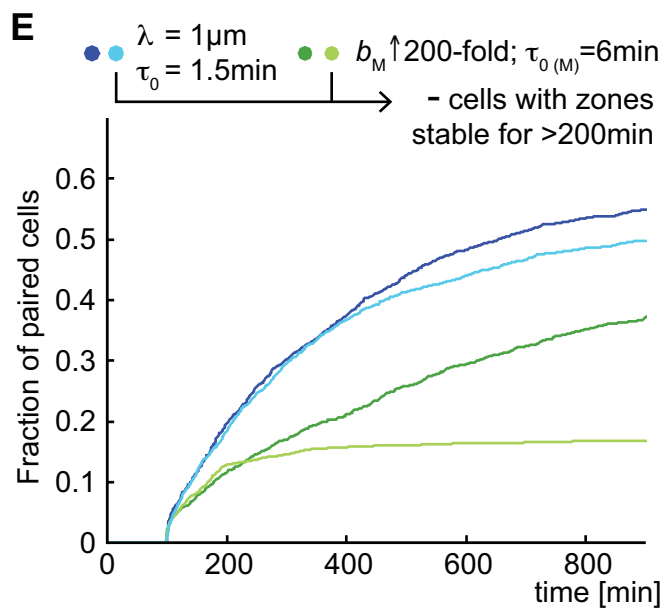
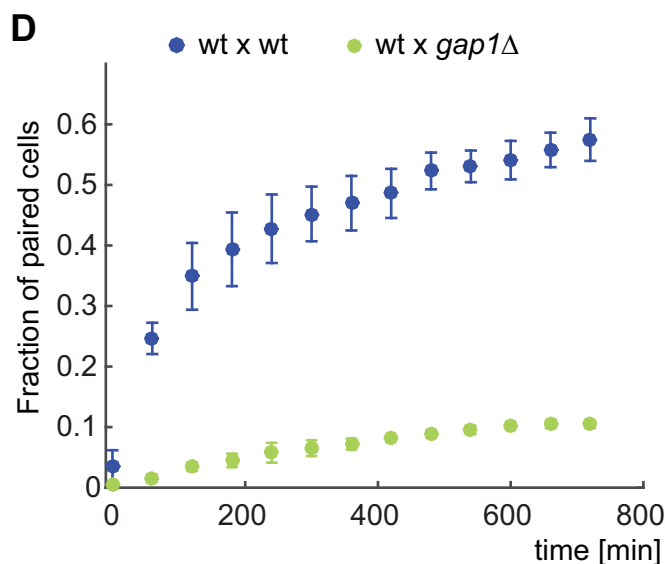
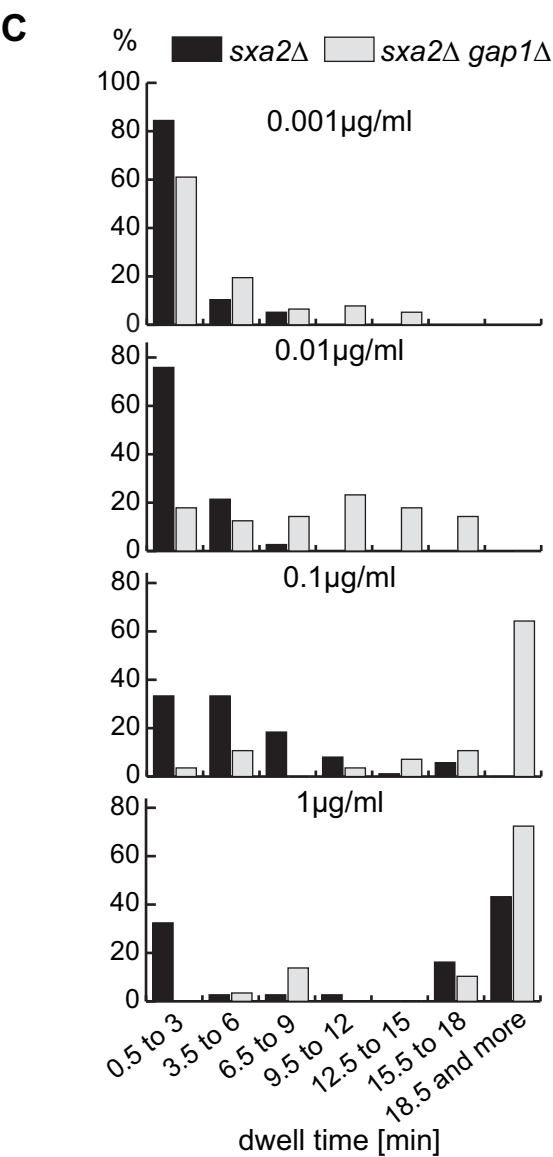
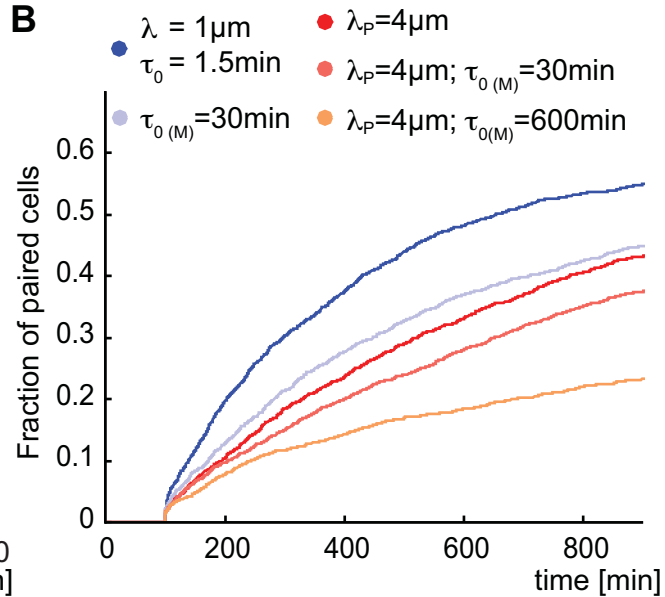
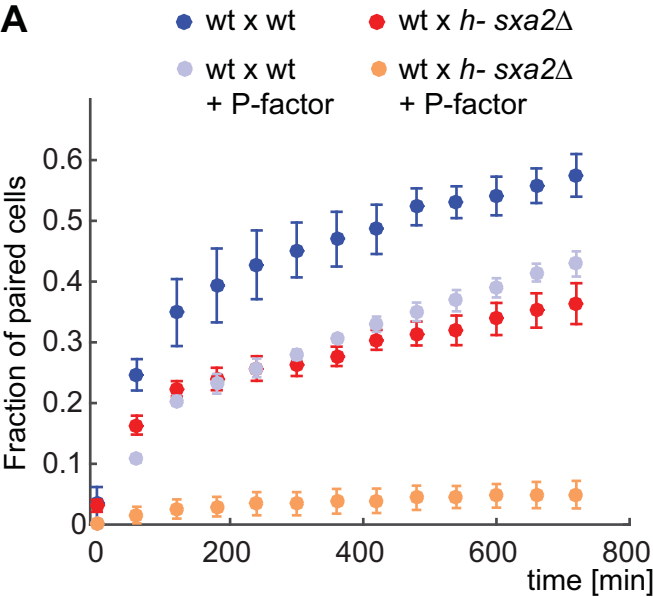
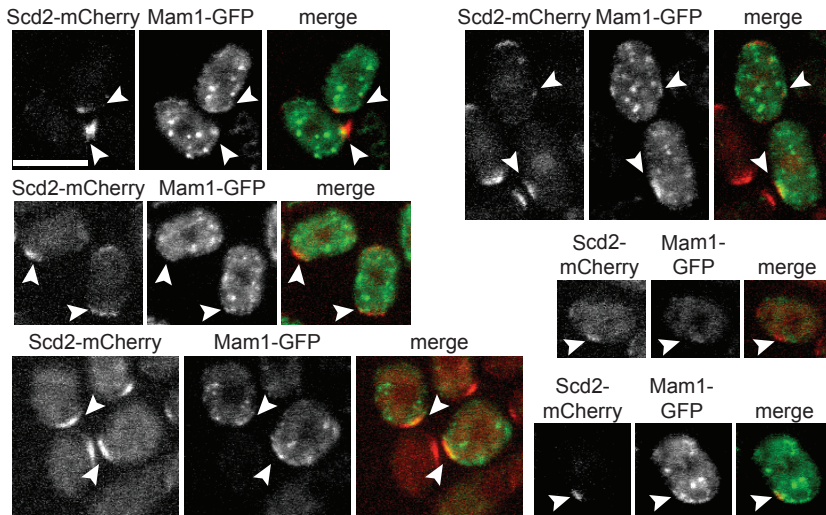
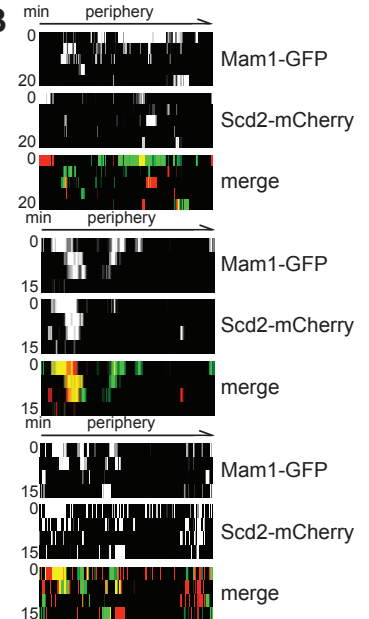


Figure S1

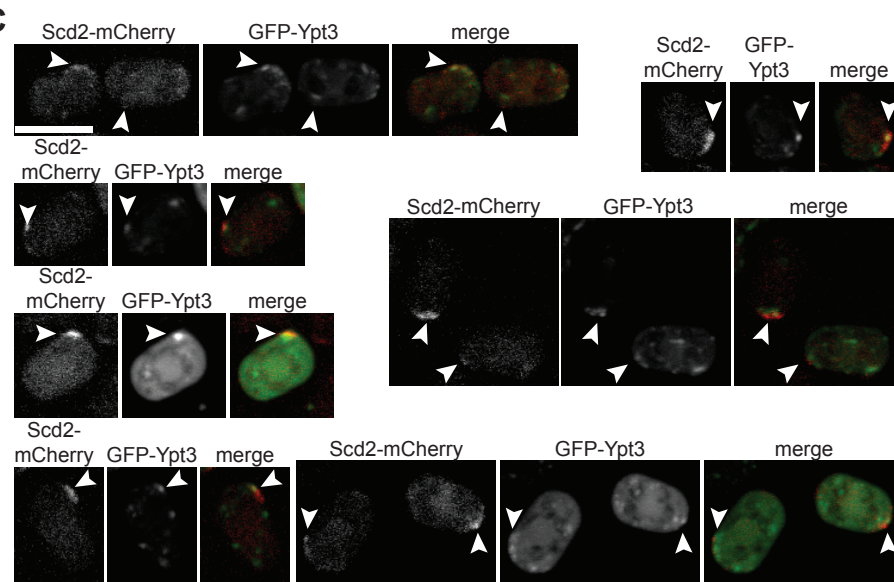
A



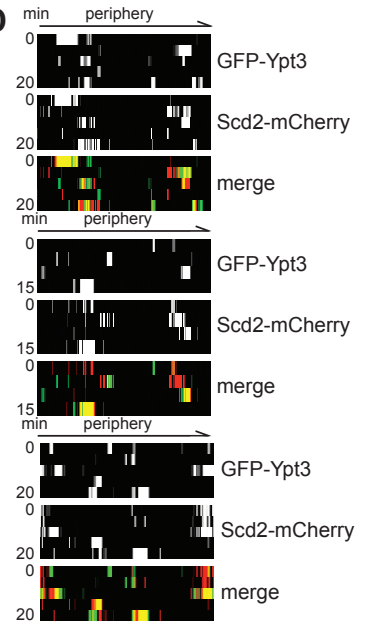
B



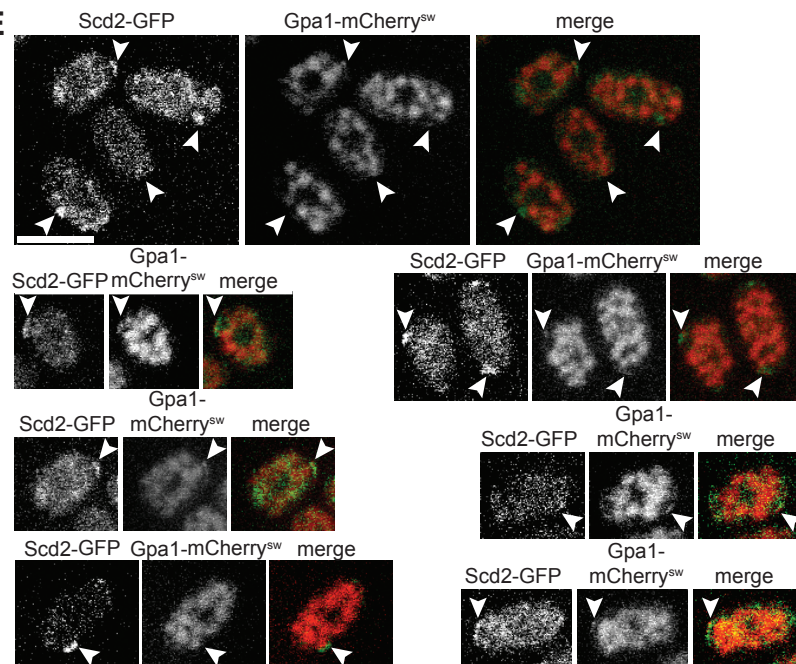
C



D



E



F

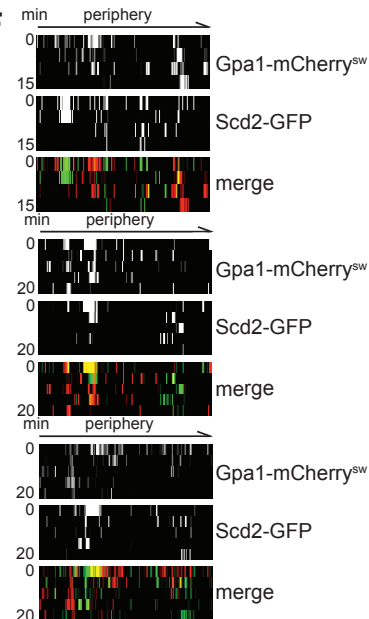


Figure S1, related to Figure 1. Localization of pheromone release and sensing machineries at polarized zones.

Spinning disk confocal projections of *h90* wild-type strains showing co-localization of Scd2-GFP and Mam1-GFP (A-B), Scd2-mCherry and GFP-Ypt3 (C-D), and Scd2-mCherry and Gpa1-mCherry^{sw} (E-F). 10 representative cells are shown for each strain (A, C, E). Kymographs of the cell periphery for 3 representative cells are shown (B, D, F). Arrowheads highlight zones of co-localization. Scale bars are 5 μ m.

Figure S2

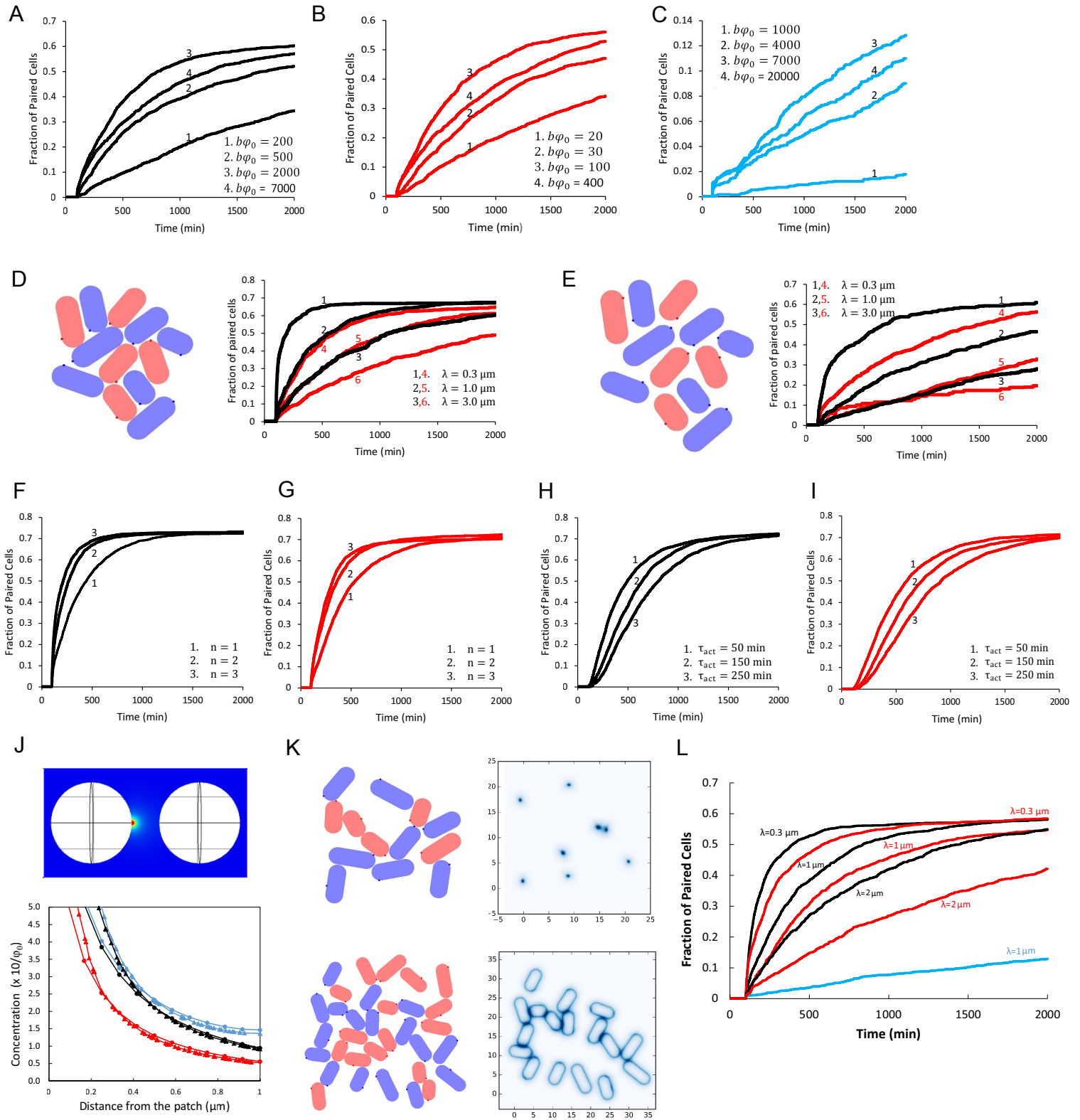
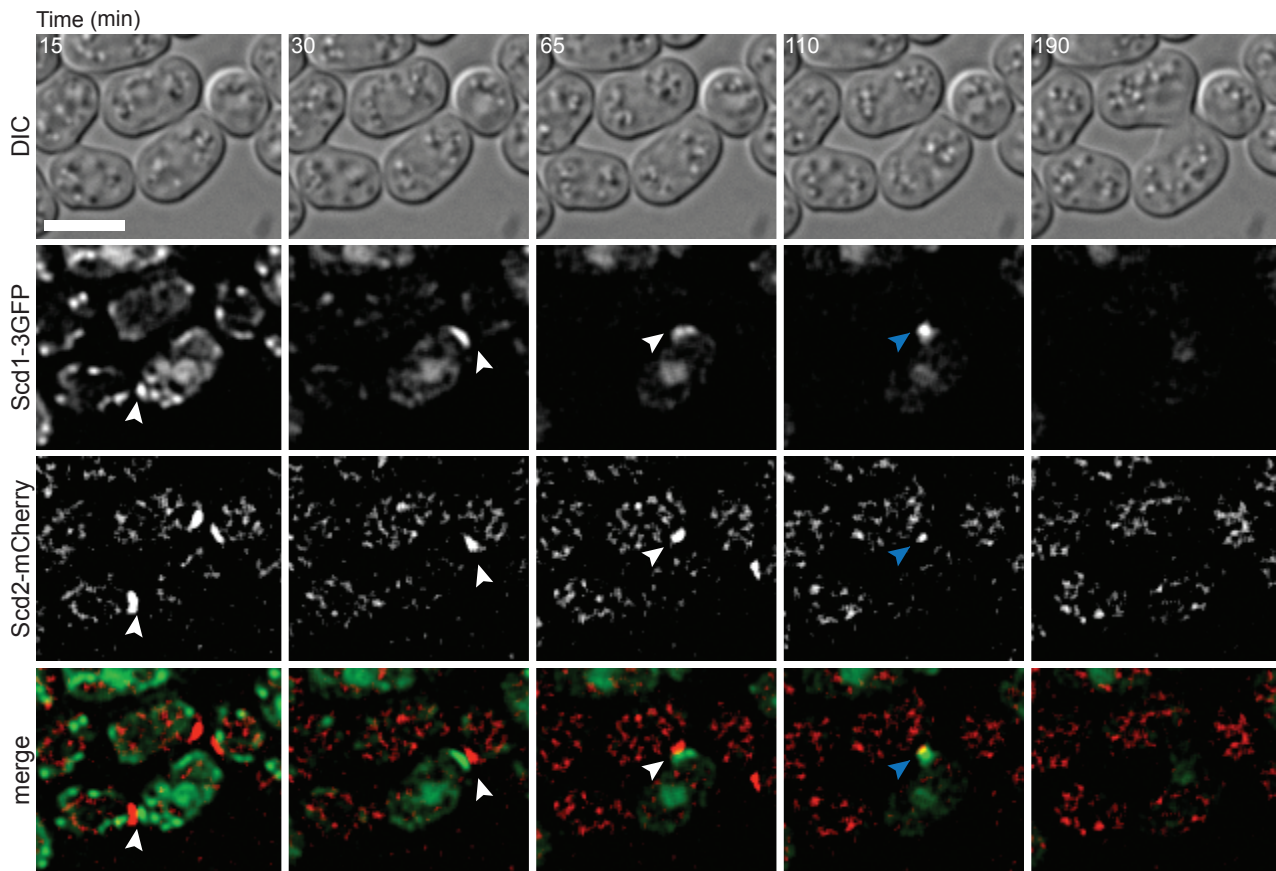


Figure S2, related to Figure 2. Dependence of results on model parameters and selection of optimal parameter values.

(A), (B) and (C) show results of simulations when scanning the sensitivity parameter b in models 1, 2 and 3. In all three graphs the third curve has the optimal value. These simulations were done using $\lambda = 1 \mu\text{m}$ and show the average in 100 simulations for 36 cells of random mating type that are placed randomly for each run as in Figure 2. (D) and (E) show how the distance between cells affect the pairing process in models 1 and 2. (D) Configuration of a group of cells touching one another and the corresponding graph of the fraction of paired cells over time, using optimized sensitivity (Model 1: $\lambda = 0.3 \mu\text{m}$: $b\varphi_0 = 45000$; $\lambda = 1 \mu\text{m}$: $b\varphi_0 = 3000$; $\lambda = 3 \mu\text{m}$: $b\varphi_0 = 1000$. Model 2: $\lambda = 0.3 \mu\text{m}$: $b\varphi_0 = 150$; $\lambda = 1 \mu\text{m}$: $b\varphi_0 = 100$; $\lambda = 3 \mu\text{m}$: $b\varphi_0 = 50$). The mating type of each cell was chosen at random in each simulation. (E) Same as panel D with similar configuration of cells but with about $1 \mu\text{m}$ distance between one another. (Model 1: $\lambda = 0.3 \mu\text{m}$: $b\varphi_0 = 50000$; $\lambda = 1 \mu\text{m}$: $b\varphi_0 = 2500$; $\lambda = 3 \mu\text{m}$: $b\varphi_0 = 1000$. Model 2: $\lambda = 0.3 \mu\text{m}$: $b\varphi_0 = 3750$; $\lambda = 1 \mu\text{m}$: $b\varphi_0 = 2500$; $\lambda = 3 \mu\text{m}$: $b\varphi_0 = 900$). Note that Model 1 (local secretion and local sensing) is more robust compared to Model 2 since its optimal sensitivity does not require a big adjustment and performs much better for $\lambda = 1 \mu\text{m}$. (F) Graph showing the effect of changing the dependence of patch life time on power n (Equation 2) for model 1. The curves for $n = 4, 5$ are close to curve for $n = 3$ and not shown. These simulations were done for $\lambda = 1 \mu\text{m}$ and show the average of 100 simulations for the set of small groups of cells in Figure 3, using optimized sensitivity ($n = 1$: $b\varphi_0 = 3000$; $n = 2$: $b\varphi_0 = 5000$; $n = 3$: $b\varphi_0 = 20000$.) (G) Same as panel F, for model 2. ($n = 1$: $b\varphi_0 = 100$; $n = 2$: $b\varphi_0 = 15$; $n = 3$: $b\varphi_0 = 0.35$.) The results of panels F and G show that nonlinear response can be used to improve the mating efficiency. This result is similar to the effect of reducing λ in Figure 2F since higher n can lead to the perception of an effectively narrower pheromone concentration profile. (H) Graph showing the effect of changing the cell activation time in Model 1. These simulations were done for $\lambda = 1 \mu\text{m}$ and show the average of 100 simulations for the set of small groups of cells in Figure 3, using the same optimized sensitivity b as in Figure 3B. (I) Same as panel H, for Model 2. Panels H and I show that longer activation time leads to slower mating kinetics, however the final fraction of mated cells does not change significantly, within the tested parameter range. (J) Calibration of 2D model accounting for cell excluded volume. Top: 3D COMSOL simulation snapshot of

concentration profile of a point source on the surface of one of two impenetrable spheres, located along the line joining their centers. The emitted signal undergoes diffusion and degradation with constant rate in the space around the two spheres. Bottom: Plots of concentration using COMSOL (triangles) versus distance away from point source for parameters that correspond to $\lambda = 1 \mu\text{m}$ and comparison with 2D model (circles). Red lines: point source profile from COMSOL in the absence of boundaries and comparison to Equation (1). Black lines: concentration profiles along the radial distance through the point source, with excluded volume of the emitting cell only, data from COMSOL and Equation (4). Blue lines: concentration profiles along the radial direction through the point source in the presence of a second sphere, with the gap between the spheres equal to $1 \mu\text{m}$, using COMSOL and Equation (4). (K) Representative pheromone profiles due to P cells using Model 1 (top) and Model 2 (bottom). (L) Same as Figure 2F but using Equation (4) instead of Equation (1) to calculate the pheromone fields. For reasons of computational efficiency, we show $\lambda = 2 \mu\text{m}$ instead of $3 \mu\text{m}$.

Figure S3



Figures S3, related to Figure 3: Dynamic behavior of polarity patches during cell pairing

Deconvolved single z-plane epifluorescence and DIC timelapse of a mixture of P and M cells expressing Scd1-3GFP and Scd2-mCherry, respectively. Cells were mixed 1:1, shifted from MSL+N to MSL-N media for 5 hours, mounted onto MSL-N agarose pad and imaged. White arrowheads highlight dynamic zones of Scd1-3GFP localization. Note that the *h+ scd1-3GFP* cell engages successively with three partners before fusing with the last one. Blue arrowheads highlight the ultimate mating partner choice. Scale bar is 5 μm .

Figure S4

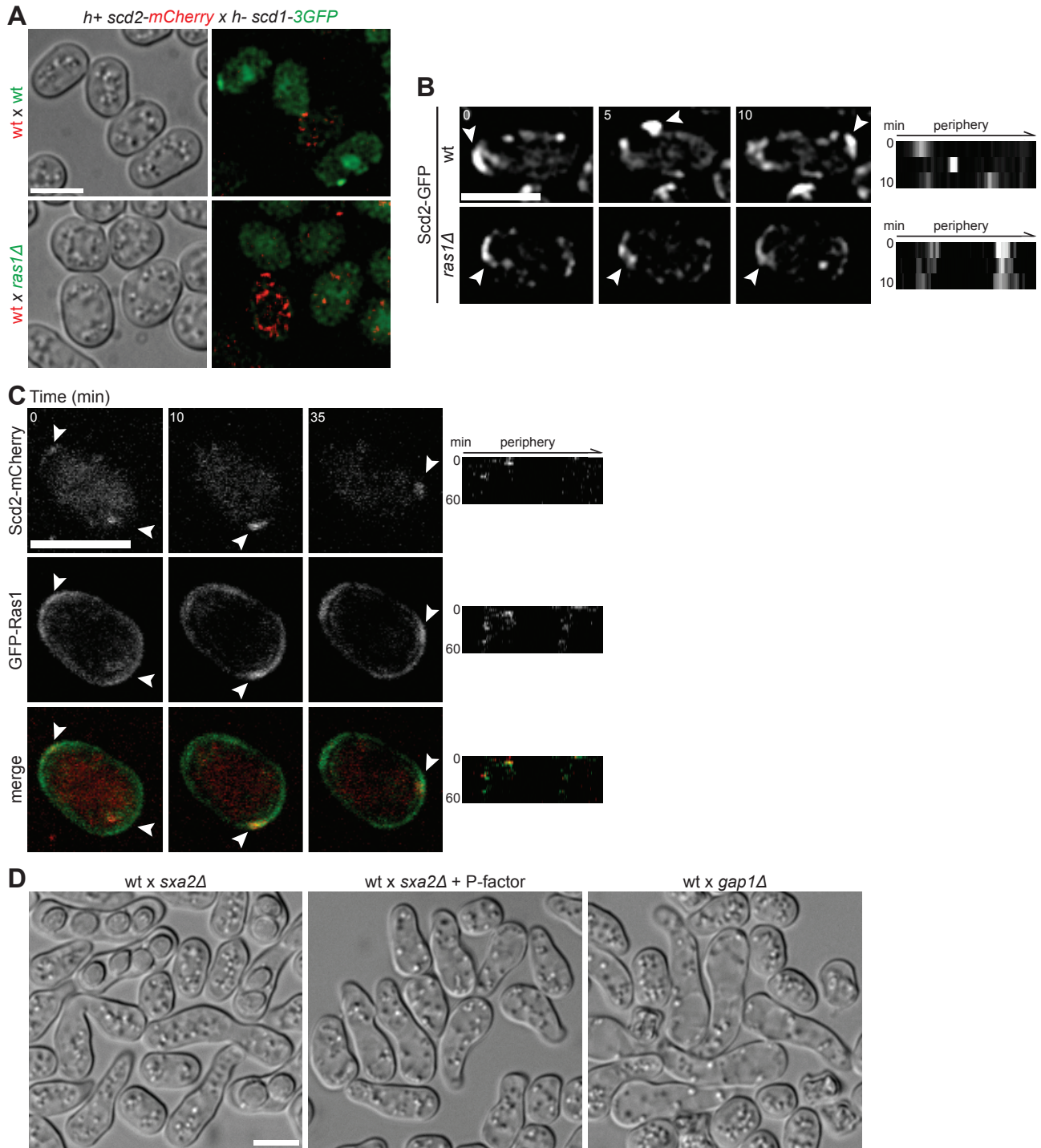


Figure S4, related to Figure 4: Ras1 is required for Scd1 localization and exploration.

(A) Deconvolved single z-plane epifluorescence and DIC images of a mixture of P and M cells with the indicated genotypes, expressing Scd2-mCherry and Scd1-3GFP, respectively. Note that the cortical Scd1-3GFP signal is essentially absent from *ras1Δ* cells. Cells were mixed 1:1, shifted from MSL+N to MSL-N media for 5 hours, mounted onto MSL-N agarose pad and imaged. (B) Deconvolved single z-plane epifluorescence images of *h-* wt and *ras1Δ* cells expressing Scd2-GFP. These were mixed with *h+* wt cells 1:1, shifted from MSL+N to MSL-N media for 5 hours, mounted onto MSL-N agarose pad and imaged. Kymographs of the cell periphery are shown on the right. Arrowheads highlight cortical Scd2-GFP zones, which are dynamic only in the wildtype cells. (C) Spinning disk confocal projections of *h90* wild-type strains showing co-localization of Scd2-mCherry and GFP-Ras1. Kymographs of the cell periphery are shown on the right. Arrowheads highlight dynamic zones of co-localization. Note that GFP-Ras1 is not restricted to these zones, but also localizes to other cortical regions. (D) DIC images of representative fields of cells at the end of a two-dimensional mating experiment on agarose pad as in Figure 4A and D. Scale bars are 5 μm.

Supplemental experimental procedures

Strains, Media, and Growth Conditions

Gene tagging was performed at the endogenous gene locus and confirmed by diagnostic PCR for both sides of the gene insertion.

All strains used in the study are described in the table below:

YSM2039	<i>h+ scd1-3GFP-kanMX</i>
YSM2042	<i>h- scd2-mCherry-natMX</i>
YSM2732	<i>h90 scd2-GFP-natMX gpa1-mCherry^{sw}-kanMX</i>
YSM2733	<i>h90 mam2-sfGFP-kanMX scd2-mCherry-natMX</i>
YSM2734	<i>h90 mam1-GFP-natMX scd2-mCherry-natMX</i>
YSM2735	<i>h90 scd2-mCherry-natMX [pREP41-GFP-ypt3]</i>
YSM2764	<i>h+ scd2-mCherry-natMX</i>
YSM2765	<i>h- scd2-GFP-natMX</i>
YSM2766	<i>h- scd2-GFP-natMX sxa2::kanMX</i>
YSM2767	<i>h+ scd2-mCherry-natMX gap1::hphMX</i>
YSM2768	<i>h- scd2-GFP-natMX sxa2::kanMX gap1::ura4+</i>
YSM2769	<i>h- scd1-3GFP-kanMX ras1::ura4+</i>
YSM2770	<i>h- scd1-3GFP-kanMX</i>
YSM2771	<i>h- scd2-GFP-natMX ras1::ura4+</i>
YSM2772	<i>h90 GFP-ras1 scd2-mCherry-natMX</i>

For experimental measurements of cell pairing, pre-cultures of YSM2039 and YSM2042 were grown in MSL +N at 25°C to OD600=0.8. Cells were diluted and mixed together to a final OD600=0.025 in MSL +N. Cells were then grown for 18 hours to OD600=0.8 at 30°C in MSL+N. Cells were harvested by centrifugation and washed 3 times in MSL -N. Cells were resuspended to OD600=1.5 in MSL -N and allowed to arrest at 30°C for 4 hours and placed onto MSL -N pad. Pads were incubated at 30°C for 1 hour before imaging. GFP and mCherry fluorescence was used to distinguish mating types.

Construction of strain expressing *gpa1*-mCherry was done as follows. First, *gpa1* was cloned with a linker consisting of -SGGSACSGAPG- following the codon for S132. PCR was done on wt chromosomal DNA to amplify *gpa1* in two parts using primer pair osm1306 (5'-tacgtcgcacccatgggatgcatgtcg) and osm1384 (5'-ccagaGCATGCGGATCCGCCAGAactattatccatagcttcaag) and pair osm1385 (5'-

tctggcggatccGCATGCTCTGGCGCGCCGGGCaatgtctctttacttccgg) and osm1386 (5'-tttCCCGGGctagagacaccattcaggg) (restriction sites are underlined, linker sequences are uppercase and start codon in italicized). The 431 bp and 976 bp products were digested with Sall and SphI, and SphI and XmaI, respectively, and both products were ligated to Sall-XmaI digested pREP41 yielding plasmid pSM1045 (pREP41-*gpa1-S132-linker*). The mCherry reading frame was then amplified from pFA6a-mCherry-natMX using primers osm947 (5'-cccggcgcgcccttgtagcagctcgtccatgc) and osm1393 (5'-ccggatccatggtgagcaagggcgaggaggataac). The product was digested with BamHI and AscI and the resulting 718 bp product was ligated to similarly treated pSM1045 yielding plasmid pSM1108 (pREP41-*gpa1-mCherry*). Next, the 3'-UTR of *gpa1* was amplified using primers osm1694 (5'-ggaattccatatgcgactctaggaaaagcctc) and osm1695 (5'-gccgtcgcaggggtggagtgtgaagcagc) and the resulting 540 bp product was digested with NdeI and Sall. The product was ligated to similarly treated pFA6a-kanMX yielding plasmid pFA6a-*gpa1-3'UTR*. The *gpa1-mCherry* gene and terminator was then amplified from pSM1108 using primers osm1306 and osm1687 (5'-acgagatctcttctaattacacaaattccg) and the resulting 3054 bp fragment was digested with Sall and BglII. The product was ligated to similarly treated pFA6a-*gpa1-3'UTR* yielding pFA6a-*gpa1-mCherry-3'UTR*. Finally, pFA6a-*gpa1-mCherry-3'UTR* was linearized by digestion with Sall and transformed into YSM1396 (*h90*) selecting for G418 resistance.

Construction of strain expressing GFP-Ras1 was done by integrating GFP-Ras1 fragment at the endogenous *ras1* locus. A linker (-TPSST-) was added between the end of GFP ORF and BamHI site. First, *ras1* 5'UTR, amplified from genomic DNA with primers osm1750 (5'-aaaactgcaggggtgccgacctcttcatgcatg) and osm1753 (5'-cctttactcatattcactattttataaagcacactaag) was stitched with GFP amplified with primers osm1751 (5'-cgggatccAGTAGAGGATGGAGTtttgatagttcatccatgcc) and osm1752 (5'-aaatagtgaaatgagtaaaggagaagaacttttcac), digested with PstI and BamHI and ligated to similarly treated *pREP41* plasmid yielding plasmid pSM1205 (*pREP41-5'UTR-GFP*). Second, *ras1* ORF and 3'UTR fragment was amplified from genomic DNA with primers osm1754 (5'-cgggatccagggtaagtctaagcaatgac) and osm1755 (5'-

tccccccgggctgcagacatagttttctatg), digested with BamHI and XmaI and ligated to similarly treated pSM1205, yielding plasmid pSM1221 (*pREP41-5'UTR-GFP-ras1-3'UTR*). Finally *5'UTR-GFP-ras1-3'UTR* fragment was excised from pSM1221 by digestion with PstI and XmaI and transformed into *ras1::ura4+* strain selecting on 5FOA plates. Restriction sites are underlined, linker sequence is uppercase, start codon is italicized and GFP sequence is bolded in osm1752 and osm1753.

Mating Assays

Except for GFP-Ypt3-expressing cells, all cells were grown in pre-culture in MSL +N at 25°C to OD600=0.6-1 and diluted to OD600=0.025 in MSL +N. Cells were then grown for 18-24 hours to OD600=0.6-1 at 30°C in MSL+N. For GFP-Ypt3 expression, cells transformed with pREP41-GFP-Ypt3 were grown in pre-culture in EMM supplemented with adenine, uracil, and thiamine (5 µg/ml) at 25°C to OD600=0.6-1 and diluted to OD600=0.025 in the same medium without thiamine to induce expression. Cells were then grown for 18-24 hours to OD600=0.6-1 at 30°C in EMM supplemented with adenine and uracil.

Cells were harvested by centrifugation and washed 3 times in MSL -N. Cells were then re-suspended in 1-3 ml MSL -N liquid medium (OD600=1.5) and incubated 3-4 h at 30°C before mounting for imaging. For imaging, cells were mounted on MSL-N agarose pads (2% agarose) that were covered with a coverslip and sealed with VALAP (1:1:1 Vaseline:Lanolin:Paraffin). To monitor the response of heterothallic *sxa2Δ* cells to different concentrations of P-factor, pads were prepared after adding the desired amount of pheromone in the melted MSL-N agarose [S1]. Cells were shifted from MSL+N to MSL-N media for 5 hours, mounted onto MSL-N agarose pad containing P-factor and imaged every 30 seconds for 20 minutes.

Computational Model

We developed a computational model for cell mating that incorporates the exploratory mechanism and Cdc42 patch stabilization of [S2]. We consider 3 models (Model 1,2,3) that all have an exploratory patch but make different

assumptions regarding the mechanism of pheromone secretion and sensing (Figure 2A). For simplicity, all models are symmetric with respect to mating cell type, except for the simulations of Figure 4 where we consider the mating of mutants and in the presence of external pheromone. The cells are represented in two dimensions as boxes of varying length, capped by semicircles at either tip (Figure 2A). This 2D representation is sufficient to capture the geometry of mating in experiments where mating occurs parallel to the glass slide. The pheromone concentration profile along the cell plane is evaluated according to reaction-diffusion laws valid in three dimensions as described below. In these equations the assumption is that the pheromone concentration profile around the cells equilibrates fast enough compared to the lifetime of the patch.

Each cell in search of a partner is assumed to contain one exploratory patch that moves around the cell periphery in discreet jumps. Since increase in pheromone concentration results in patch stabilization (Figure 2B; [S2]), we assume that the residence time of the patch increases with concentration of sensed opposite-type pheromone. Cells are assumed to mate and are taken out of the simulation when (i) they have their patches oriented in such a way as to allow their fusion by shmoo extension and (ii) have remained thus engaged for a time longer than τ_{pairing} , namely the time after which cells would have formed a shmoo and mated.

The simulation is advanced by time dt at each step. At each step the probability of patch motion is evaluated. The correspondence to experimental time is established by setting the patch motion probability to dt/τ , where τ is the average zone lifetime. Cell fusion is assumed to occur when cell pairs exist for $\tau_{\text{pairing}} = 100$ min, which corresponds to τ_{pairing}/dt simulation steps.

In more detail, the components of the three models are as follows:

Pheromone concentration profiles

In Models 1 and 3 the pheromone is assumed to be secreted locally at the site of each Cdc42 patch i , \mathbf{r}_i . Assuming uniform degradation by proteases in the bulk outside of the cells, the steady state concentration at location \mathbf{r} due to a patch of a P ($h+$) cell is given by [S3, S4]:

$$\varphi_{h+}^i(\mathbf{r}) = \varphi_0 d \frac{e^{-|\mathbf{r}-\mathbf{r}_i|/\lambda}}{|\mathbf{r}-\mathbf{r}_i|+d}, \quad (1)$$

where φ_0 is a reference concentration value that depends on the rate of pheromone secretion at the patch, λ is a decay length arising from a uniform degradation rate by proteases, and $d = 0.1 \mu\text{m}$ is a small-scale parameter that prevents the concentration from reaching infinity due to the finite size of the patch. The decay length depends on the diffusion coefficient of the pheromone D and the degradation rate g : $\lambda = \sqrt{D/g}$ [S4]. The total concentration of P-factor at location \mathbf{r} is found by summing over the contributions of all P-cell patches. Identical expressions are used for the M-factor concentration fields.

The expression in Equation (1) does not account for the effects of cell-excluded volume, which may lead to accumulation of pheromone secreted in the narrow space between neighboring cells. The effect of cell-excluded volume was considered in a separate set of simulations described below.

In Model 2 we assume uniform pheromone secretion. For this model, instead of using a single pheromone source per cell, we instead uniformly distribute pheromone sources around the cell body and cell tips, separated by 0.23-0.26 μm .

When a patch changes location, for numerical efficiency, we only update the concentration values close to the old and new patch locations over a distance 4λ . A larger range of 12λ was used for simulations of cells that were very sensitive to small pheromone concentrations in Fig. 4E

Sensing and patch exploratory kinetics

To simulate the patch exploration process, we assume that each patch has an average lifetime τ , with an exponential distribution of lifetimes. When a patch moves, it is placed randomly along the boundary of the cell tip or cell body, with a probability 0.82 to be on a cell tip as compared to the cell body, as measured in [S2]. The same statistics were used for the initial placement of the patch, except for the simulations of Figure 4 (see last paragraph of this sub-section).

In models 1 and 2 we assume that the opposite-type pheromone is sensed at the patch location. The lifetime of a patch of a P-cell at location \mathbf{r}_{patch} is given by:

$$\tau = \tau_0 \left\{ 1 + \left[b \varphi_{h-}(\mathbf{r}_{patch}) \right]^n \right\}, \quad (\text{Models 1,2}) \quad (2)$$

and similarly for M-cells. Here $\varphi_{h-}(\mathbf{r}_{patch})$ is the local concentration of M-factor, b measures the magnitude of the response to the sensed pheromone, and $\tau_0 = 1.5$ min is the patch residence time in the absence of nearby cells [S2]. The exponent n is included to allow for a nonlinear sensing mechanism. The Figures in the main text show the simplest case of linear dependence, $n=1$.

The expression for patch movement in Model 3 (uniform sensing) is the same as in Equation (2), however we use the average pheromone concentration around the boundary of the cell body and cell tip, $\langle \varphi_{h-} \rangle$, to evaluate the patch lifetime:

$$\tau = \tau_0 \left\{ 1 + \left[b \langle \varphi_{h-} \rangle \right]^n \right\}, \quad (\text{Model 3}) \quad (3)$$

The patch lifetime and movement probability is re-evaluated on every time step of the simulation, dt (typically 0.2 min). Here we assume that the sensing and patch stabilization mechanism adjusts fast compared to the time of patch movement, thus allowing us to neglect memory effects.

The initial position of the patch does not affect the simulation outcome significantly: in simulations of wild type cells, cells typically find their partners through a few rounds of exploration. When simulating cells with larger lifetimes or perceiving higher pheromone (protease and *gap1Δ* experiments in Figure 4), the initial position of the domain was set at the cell poles. This was done (i) to ensure that the poor mating statistics is not due to poor initial domain location, and (ii) because initial zones in experiments often appear at cell poles.

Cell engagement

Cells with patches stabilized at the same cortical position for a long time extend shmoos; cell fusion follows if these shmoos encounter a shmoo from an opposite mating type [S5]. Shmoos are able to turn and adjust their orientation as they grow towards a partner. We accounted for this process in the simulations by the

following procedure. For every patch and for every time step of the simulation we find if a patch of the opposite mating type exists within a selection zone (Figure 2C). The selection zone, which is an approximation of the region that a growing shmoo would be able to reach by extension and turning consists of: a circle centered at the Cdc42 patch with radius equal to $0.3 w$, where $w = 3.4 \mu\text{m}$ is cell width, plus a cone of angle 60° for distances between $0.3 w$ to $0.5 w$, plus a cone of angle 30° for distances between $0.5 w$ to $2 w$. The cone apices are at the patch positions and the axes of the cones are normal to the cell contour. No mating is allowed for distances larger than $2 w$. If a patch of opposite type exists within the selection zone then the cell is considered “engaged”. Two cells that remain mutually engaged for a time longer than τ_{pairing} are assumed to mate and are taken out of the simulation (Figure 2C).

Search activation and cell lysis

In the simulations of Figure 2D-F, all cells are assumed to be in the exploratory phase at the start of the simulation. To simulate the effect of cells entering the exploratory phase at different point in time, we also allowed cells to become active at random, according to an exponential distribution of average time τ_{act} (Figure S2H, I). Inactive cells in the simulation do not have patches so they cannot mate or secrete pheromone.

To account for the effects of unproductive projection formation or lysis of gap1 Δ cells, in Figure 4E we took out from the simulation cells with patches that have been stable at the same location for more than 200 min.

Cell placement

Our program allows the user to specify the location, mating type and number of cells within a simulation box. These properties can also be assigned at random. In simulations of large fields of cells (Figure 2F) cells were placed at random positions according to the following process.

A defined number of candidate cell locations and orientations were picked from a random distribution. Those cells that happen to be at locations within one cell width distance to one another are eliminated. The remaining cells were grown with a uniform rate up to 8 μm , or less, in case further growth would lead to an overlap with another cell. To allow for a tighter packing comparable to experiments, a slight translation and rotation by a small angle was applied when cells collided. Typical configurations are shown in Figure 2D.

Simulations accounting for cell excluded volume in pheromone profiles

The pheromone concentration expression of Equation (1) assumes free diffusion and spatially uniform degradation. Cell-excluded volume influences how the pheromone diffuses away from an emitting cell in 3D, in the presence of neighboring cells. While the geometry of cells near the site of patch secretion can be specified, the computational time required to solve the boundary value problem at every time step in 3D is extremely long for the purposes of this work. We thus developed an iterative procedure to account for cell crowding in our 2D simulations.

To account for the reflection of pheromone at cell boundaries, we added fictitious point pheromone sources along cell boundaries. These point sources were distributed uniformly at positions \mathbf{r}_j along each 2D cell boundary, separated by 0.125-0.131 μm . The strength of the reflective sources was assumed proportional to the pheromone arriving from a distant patch i , in the absence of boundaries. The expression used to calculate the pheromone concentration at position \mathbf{r} due to a patch of an $h+$ cell located at \mathbf{r}_i was:

$$\begin{aligned} \varphi_{h+}^{i, \text{with reflection}}(\mathbf{r}) = & \varphi_{h+}^i(\mathbf{r}) + \sum_j \varepsilon \varphi_{h+}^i(\mathbf{r}_j) d \frac{e^{-|\mathbf{r}-\mathbf{r}_j|/\lambda}}{|\mathbf{r}-\mathbf{r}_j| + d} \\ & + \sum_k \sum_j \varepsilon^2 \varphi_{h+}^i(\mathbf{r}_j) d \frac{e^{-|\mathbf{r}_k-\mathbf{r}_j|/\lambda}}{|\mathbf{r}_k-\mathbf{r}_j| + d} \times d \frac{e^{-|\mathbf{r}-\mathbf{r}_k|/\lambda}}{|\mathbf{r}-\mathbf{r}_k| + d} \quad (4) \end{aligned}$$

Here φ_{h+}^i is the pheromone field given by Equation (1) in the absence of cell boundaries, ε is a proportionality constant and the sum is over all cell points along the 2D cell boundaries, including those on the secreting cell (we only consider points within 4λ of a source). The term with two sums represents the secondary reflection of the first reflection.

We found that $\varepsilon = 0.15$ gave a good approximation for the pheromone profile in between two cells separated by 0.5 and 1 μm and $\lambda = 0.3, 0.6, 2,$ and 3 μm by comparing to the 3D solution found using COMSOL (Figure S2J). For this value of ε , the term with the two sums provides an overall contribution smaller in magnitude compared to the other terms. The COMSOL simulation included two spheres of diameter equal to the cell diameter and a point source located on the boundary. The point source was assumed to emit pheromone at constant rate, diffusing with diffusion coefficient $D = 300 \mu\text{m}^2/\text{sec}$ [S4]. A uniform degradation rate g was used to generate $\lambda = \sqrt{D/g}$ for comparison to the value of λ used in the 2D model. The COMSOL domain covered a box of size 4 x 4 x 7.5 μm around the center between the two spheres, with open boundary conditions at its sides. To find a good value for ε we first found the concentration rescaling factor between COMSOL and Equation (1) by matching the amplitudes at a distance 0.28 μm from a point source, in the absence of any boundary. We then found a value of ε that results in a good approximation to the pheromone profile along the radial direction going through the patch, in the presence of absence of a neighboring cell (Figure S2J). Representative images of the concentration profiles for $\lambda = 1 \mu\text{m}$ for the models with local and uniform secretion are shown in Figure S2K.

While the above procedure includes various unavoidable approximations, it allowed us to check that our predicted dependence of the mating kinetics on parameter λ (Figure 2F) is maintained when accounting for the effects of excluded volume, even though the precise shape of the mating curves is mildly affected (Figure S2L).

Supplemental references

- S1. Vjestica, A., Merlini, L., Dudin, O., Bendezu, F.O., and Martin, S.G. (2016). Microscopy of Fission Yeast Sexual Lifecycle. *J. Vis. Exp.*
- S2. Bendezu, F.O., and Martin, S.G. (2013). Cdc42 Explores the Cell Periphery for Mate Selection in Fission Yeast. *Curr Biol* 23, 42-47.
- S3. Barkai, N., Rose, M.D., and Wingreen, N.S. (1998). Protease helps yeast find mating partners. *Nature* 396, 422-423.
- S4. Rappaport, N., and Barkai, N. (2012). Disentangling signaling gradients generated by equivalent sources. *Journal of biological physics* 38, 267-278.
- S5. Dudin, O., Bendezu, F.O., Groux, R., Laroche, T., Seitz, A., and Martin, S.G. (2015). A formin-nucleated actin aster concentrates cell wall hydrolases for cell fusion in fission yeast. *J Cell Biol* 208, 897-911.